

X-ray Diffraction Techniques to Characterize Liquid Surfaces and Monomolecular Layers at Gas-Liquid Interfaces

David Vaknin

Ames Laboratory and Department of Physics and Astronomy, Iowa State University, Ames, Iowa 50011, USA

(December 2, 2024)

I. INTRODUCTION

X-ray and neutron scattering techniques are probably the most effective tools to be employed in order to determine the structure of liquid interfaces on molecular length scales. These are not different in principle from conventional X-ray diffraction techniques that are usually applied to three dimensional crystals, liquids, solid surfaces etc. However, special diffractometers that enable scattering from fixed horizontal surfaces are required to carry out the experiments. Indeed, systematic studies of liquid surfaces had not begun until the introduction of the first liquid surface reflectometer. [1].

A basic property of a liquid-gas interface is the length scale over which the molecular density changes from the bulk value to that of the homogeneous gaseous medium. Molecular size and capillary waves, that depend on surface tension and gravity, are among the most important factors that shape the density profile across the interface and the planar correlations [14,9,49]. In some instances the topmost layers of liquids are packed differently than in the bulk, giving rise to layering phenomena at the interface. Monolayers of compounds different than the liquid can be spread at the gas-liquid at interface, and are termed Langmuir monolayers [17,50]. The spread compound might *wet* the liquid surface to form a film of homogeneous thickness or cluster to form an inhomogeneous *rough* surface. The X-ray reflectivity (XR) technique allows one to determine the electron density across such interfaces from which the molecular density and the total thickness can be extracted. The grazing angle diffraction (GID) technique is commonly used to determine lateral arrangements and correlations of the topmost layers at interfaces. GID is especially efficient in cases where surface crystallization of the liquid or spread monolayers occurs. Both techniques (XR and GID) provide structural information that is averaged over macroscopic areas in contrast to scanning probe microscopies (SPM's) where local arrangements are probed. For an inhomogeneous interface the reflectivity is an incoherent sum of reflectivities, accompanied by strong diffuse scattering which in general is difficult to interpret with definitive answers and often requires complementary techniques to support the X-ray analysis. Therefore, preparation of well-defined homogeneous interfaces is a key to a more definitive and straightforward interpretation.

A. Competitive and Related Techniques

Although modern scanning probe microscopies (SPM's) such as scanning tunneling microscopy (STM) [5] and atomic force microscopy (AFM) [6] rival X-ray scattering techniques

in probing atomic arrangements of solid surfaces, they have not yet become suitable techniques for free liquid surfaces. The large fluctuations due to the two-dimensional nature of the liquid interface, high molecular mobility, and the lack of electron conductivity (which is necessary for STM) are among some of the main obstacles that make it difficult to apply these techniques to gas-liquid interfaces. In dealing with volatile liquids, inadvertent deposition or wetting of the probe by the liquid can occur which may obscure the measurements. In addition, the relatively strong interaction of the probe with the surface might alter its pristine properties. For similar and other reasons, electron microscopy and electron diffraction techniques, which are among the best choices for probing solid surfaces, are not suitable to most liquid surfaces, and in particular aqueous interfaces. On the other hand, visible light microscopy techniques such as Brewster angle microscopy (BAM) [3,19,20] or fluorescence microscopy [28] have been used very successfully in providing morphological pictures of the interface on the micrometer length scale. This information in general, is complementary to that extracted from X-ray scattering. These techniques are very useful for characterizing inhomogeneous surfaces with two or more distinct domains for which XR and GID results are usually difficult to interpret. However, it is impossible to determine the position of the domains with respect to the liquid interface, their thicknesses or their chemical nature. Ellipsometry is another technique that exploits visible light, to allow determination of film thickness on a molecular length scale and assumes that one knows the refractive index of the substrate and of the film [3,12]; either might be different from their bulk values and difficult to determine.

In the following sections theoretical background to the X-ray techniques is presented together with experimental procedures and data analysis concerning liquid surfaces. It is intended to provide a basic formulation which can be developed for further specific applications. Several examples of these techniques applied to a variety of problems are presented briefly to demonstrate the strengths and limitations of the techniques. It should be borne in mind that the derivations and procedures described below are mostly general and can be applied to solid surfaces, and *vice-versa*, many results applicable to solid surfaces can be used for liquid surfaces. X-ray reflectivity from surfaces and GID have been treated in recent reviews [2,43,61].

II. THEORETICAL BACKGROUND

We assume that a plane harmonic wave of frequency ω and wave-vector \mathbf{k}_0 (with electric field, $\mathbf{E} = \mathbf{E}_0 e^{i\omega t - i\mathbf{k}_0 \cdot \mathbf{r}}$) is scattered from a distribution of free electrons, with a number density $N_e(\mathbf{r})$. Due to the interaction with the electric field of the X-ray wave, each free electron experiences a displacement proportional to the electric field, $\mathbf{X} = -\frac{e}{m\omega^2} \mathbf{E}$. This displacement gives rise to a polarization $\mathbf{P}(\mathbf{r})$ distribution vector

$$\mathbf{P}(\mathbf{r}) = N_e(\mathbf{r}) e \mathbf{X} \quad (1)$$

in the medium. For the sake of convenience we define the scattering length density (SLD) $\rho(\mathbf{r})$ in terms of the classical radius of the electron $r_0 = \frac{e^2}{4\pi\epsilon_0 m c^2} = 2.82 \times 10^{-13}$ cm as follows

$$\rho(\mathbf{r}) = N_e(\mathbf{r}) r_0 \quad (2)$$

The polarization then can be written as

$$\mathbf{P}(\mathbf{r}) = -\frac{N_e(\mathbf{r})e^2}{\omega^2 m_e} \mathbf{E} = -\frac{4\pi\epsilon_0}{k_0^2} \rho(\mathbf{r}) \mathbf{E} \quad (3)$$

The scattering length density (or the electron density) is what we wish to extract from reflectivity and GID experiments and relate it to atomic or molecular positions at liquid interfaces. The displacement vector \mathbf{D} can now be constructed as follows:

$$\mathbf{D} = \epsilon(\mathbf{r}) \mathbf{E} + \mathbf{P}(\mathbf{r}) = \epsilon(\mathbf{r}) \mathbf{E} \quad (4)$$

where $\epsilon(\mathbf{r})$ is the permittivity of the medium usually associated with the refractive index $n(\mathbf{r}) = \sqrt{\epsilon(\mathbf{r})}$. To account for absorption by the medium we introduce a phenomenological factor β that we calculate from the linear absorption coefficient μ , (given in tables [21]) as follows $\beta = \mu/(2k_0)$. Then the most general permittivity for X-rays becomes

$$\epsilon(\mathbf{r}) = \epsilon_0 [1 - \frac{4\pi}{k_0^2} \rho(\mathbf{r})] + 2i\beta \quad (5)$$

Typical values of the SLD (ρ) and the absorption term (β) for water and liquid mercury are listed in Table I. In the absence of true charges in the scattering medium (i.e., a neutral medium) and under the assumption that the medium is nonmagnetic (magnetic permeability $\mu = 1$) the wave equations that need to be solved to predict the scattering from a known SLD can be derived from the following Maxwell equations [35],

$$\begin{aligned} \nabla \cdot \mathbf{D} &= 0 & \nabla \cdot \mathbf{H} &= 0 \\ \nabla \times \mathbf{E} &= -\partial \mathbf{H} / \partial t & \nabla \times \mathbf{H} &= \partial \mathbf{D} / \partial t. \end{aligned} \quad (6)$$

Under the assumption of harmonic plane waves, $\mathbf{E} = \mathbf{E}_0 e^{i\omega t - i\mathbf{k} \cdot \mathbf{r}}$, the following general equations are obtained from Eq. 6:

$$\nabla^2 \mathbf{E} + [k_0^2 - 4\pi\rho(\mathbf{r})] \mathbf{E} = -\nabla (\nabla \ln \epsilon(\mathbf{r}) \cdot \mathbf{E}), \quad (7)$$

$$\nabla^2 \mathbf{H} + [k_0^2 - 4\pi\rho(\mathbf{r})] \mathbf{H} = -\nabla \ln \epsilon(\mathbf{r}) \times (\nabla \times \mathbf{H}). \quad (8)$$

In some particular cases the right hand side of Equations 7 and 8 is zero. We notice then, that the term $4\pi\rho(\mathbf{r})$ in the equation plays a role similar to that of a potential $V(\mathbf{r})$ in wave mechanics. In fact, for most practical cases the right hand side of Equations 7 and 8 can be approximated to zero, thus the equation for each component of the fields resembles a stationary wave equation. In those cases general mathematical tools, such as the Born approximation (BA) and the distorted wave Born approximation (DWBA) can be used [47].

A. Reflectivity

In reflectivity experiments a monochromatic X-ray beam of wavelength λ [wavevector $k_0 = 2\pi/\lambda$ and $\mathbf{k}_i = (0, k_y, k_z)$] is incident at an angle α_i on a liquid surface and is detected at an outgoing angle α_r such that $\alpha_i = \alpha_r$, as shown in Figure 1, with a final wave vector \mathbf{k}_f . The momentum transfer is defined in terms of the incident and reflected beam as follows,

$$\mathbf{Q} = \mathbf{k}_i - \mathbf{k}_f, \quad (9)$$

where in the reflectivity case \mathbf{Q} is strictly along the surface normal, with $Q_z = 2k_0 \sin \alpha = 2k_z$.

1. Single, Ideally Sharp Interface - Fresnel Reflectivity

Solving the scattering problem exactly for the ideally sharp interface although simple, is very useful for the derivation of more complicated electron density profiles across interfaces. The wavefunctions employed are also essential for inclusion of dynamical effects when dealing with non-specular scattering i.e., GID and diffuse scattering.

1a. s-polarized X-ray beam

For a stratified medium with an electron density that varies along one direction, z , ($\rho(\mathbf{r}) = \rho(z)$ assuming no absorption i.e., $\beta = 0$), an s-type polarized X-ray beam with the electric field parallel to the surface (along the x-axis, see Fig. 1) obeys the stationary wave equation as derived from Eq. 7 and is simplified as follows,

$$\nabla^2 E_x + [k_0^2 - V(z)]E_x = 0, \quad (10)$$

with an effective potential $V(z) = 4\pi\rho(z)$. The general solution to Eq. 2 is then given by,

$$E_x = E(z)e^{ik_y y} \quad (11)$$

where the momentum transfer along y is conserved when the wave travels through the medium leading to the well-known Snell's rule for refraction. Inserting Eq. 11 in Eq. 10 leads to a one dimensional wave equation through a potential $V(z)$,

$$\frac{d^2 E}{dz^2} + [k_z^2 - V(z)]E = 0. \quad (12)$$

The simplest case of Eq. 12 is that of an ideally flat interface, separating the vapor phase and the bulk scattering length density ρ_s , at $z = 0$. The solution of Eq. 12 is then given by

$$E(z) = \begin{cases} e^{ik_{z,0}z} + r(k_{z,s})e^{-ik_{z,0}z} & z \geq 0 \text{ in gas} \\ t(k_{z,s})e^{ik_{z,s}z} & z \leq 0 \text{ in liquid} \end{cases} \quad (13)$$

where

$$k_{z,s} = \sqrt{k_{z,0}^2 - 4\pi\rho_s} = \sqrt{k_{z,0}^2 - k_c^2}, \quad (14)$$

where $k_c \equiv 2\sqrt{\pi\rho_s}$. By applying continuity conditions to the wavefunctions and to their derivatives at $z = 0$, the Fresnel equations for reflectance, $r(k_{z,s})$, and transmission, $t(k_{z,s})$, are obtained,

$$r(k_{z,s}) = \frac{k_{z,0} - k_{z,s}}{k_{z,0} + k_{z,s}}, \quad t(k_{z,s}) = \frac{2k_{z,0}}{k_{z,0} + k_{z,s}}. \quad (15)$$

The measured reflectivity from an ideally flat interface, R_F , is usually displayed as a function of the momentum transfer $Q_z = k_{z,0} + k_{z,s} \approx 2k_{z,0}$, and is given by

$$R_F(Q_z) = |r(k_{z,s})|^2. \quad (16)$$

Below a critical momentum transfer, $Q_c \equiv 2k_c \equiv 4\sqrt{\pi\rho_s}$, $k_{z,s}$ is an imaginary number and $R_F(Q_z) = 1$; total external reflection occurs. Notice that whereas the critical momentum

transfer does not depend on the X-ray wavelength, the critical angle for total reflection does, and it is given by $\alpha_c \approx \lambda \sqrt{\rho_s/\pi}$. Typical values for critical angles for X-rays of wavelength $\lambda_{CuK_\alpha} = 1.5404\text{\AA}$, are listed in Table I. For $Q_z \gg Q_c$, $R_F(Q_z)$ can be approximated to a form that is known as the Born approximation,

$$R_F(Q_z) \sim \left(\frac{Q_c}{2Q_z} \right)^4. \quad (17)$$

This form of the reflectivity at large Q_z 's is also valid for internal scattering, i.e., reflectivity from liquid into the vapor phase. However, total reflection does not occur for the internal reflectivity case. Calculated external and internal reflectivity curves from an ideally flat surface, R_F , displayed versus momentum transfer (in units of the critical momentum transfer) are shown in Fig. 2(a). Both reflectivities converge at large momentum transfer where they can be both approximated by Eq. 17. The dashed line in the same figure shows the approximation $(Q_c/2Q_z)^4$, which fails in describing the reflectivity close to the critical momentum transfer.

The photon transmission at a given $k_{z,s}$ is given by

$$T(k_{z,s}) = |t(k_{z,s})|^2 \frac{\text{Re}(k_{z,s})}{\text{Re}(k_{z,0})}. \quad (18)$$

where the ratio on the right hand side accounts for the flux through the sample. In the case of external reflection, and for values of $k_{z,0}$ that are smaller than k_c , the real part of $k_{z,s}$ is zero, and there is no transmission, whereas above the critical angle $k_{z,s}$ is real, and the transmission is given by,

$$T(k_{z,s}) = \frac{4k_{z,0}k_{z,s}}{(k_{z,0} + k_{z,s})^2} \text{ for } k_{z,0} > k_c \quad (19)$$

and the conservation of photons is fulfilled in the scattering process,

$$T(k_{z,s}) + R(k_{z,s}) = 1. \quad (20)$$

In Fig. 2(b) the transmission amplitude $|t(k_{z,s})|$ for external (solid line) and for internal (dashed line) reflections are shown. This amplitude modulates non-specular scattering processes at the interface as will be discussed later in this unit.

The effect of absorption on the reflectivity can be incorporated by introducing β into the generalized potential in Eq. 11, so that $k_{z,s} = \sqrt{k_{z,0}^2 - k_c^2 + 2i\beta}$ is used in the Fresnel equations Eq. 15. Calculated reflectivities from water and liquid mercury demonstrating that the effect of absorption is practically insignificant for the former yet has the strongest influence near the critical angle for the latter, are shown in Fig. 3.

2. Multiple Stepwise and Continuous Interfaces

On average, the electron density across a liquid interface is a continuously varying function, and is a constant far away on both sides of the interface, as is shown in Fig. 4.

The reflectivity for a general function $\rho(z)$ can be then calculated by one of several methods classified into two major categories: *dynamical* and *kinematical* solutions. The dynamical solutions are in general more exact and include all the features of the scattering, in particular the low angle regime, close to the critical angle where multiple scattering processes occur. For a finite number of discrete interfaces exact solutions can be obtained by use of standard recursive [36] or matrix [7] methods. These methods can be extended to compute with very high accuracy the scattering from any continuous potential by *slicing* it into a finite but with sufficient number of interfaces. On the other hand, the kinematical approach neglects multiple scattering effects and fails in describing the scattering at small angles.

2a. The Matrix Method

In this approach the scattering length density with variation over a characteristic length d_t is *sliced* into a histogram with N interfaces. The matrix method, is practically equivalent to the Parratt formalism [7]. For each interface, the procedure described previously for the one interface is applied. Consider an arbitrary interface, n , separating two regions, of a *sliced* SLD (as in Fig. 4), with ρ_{n-1} , and ρ_n at position $z = z_n$ with the following wavefunctions

$$\begin{array}{ccc} \rho_{n-1} & & \\ R_{n-1,n} e^{-ik_{n-1}z} & \leftarrow & \rho_n \\ T_{n-1,n} e^{ik_{n-1}z} & \rightarrow & R_{n,n+1} e^{-ik_n z} \\ & & \left| \begin{array}{ccc} & \leftarrow & \\ & \rightarrow & \\ z = z_n & & \end{array} \right. \\ & & T_{n,n+1} e^{ik_n z} \\ & & R_{n,n+1} \end{array} \quad (21)$$

where $k_n \equiv \sqrt{k_{z,0}^2 - 4\pi\rho_n}$. The effect of absorption can be taken into account as described earlier. For simplicity, the subscript z is omitted from the component of the wavevector so that $k_{z,n} = k_n$. The solution at each interface in terms of a transfer matrix, M_n , is given by

$$\begin{pmatrix} T_{n-1,n} \\ R_{n-1,n} \end{pmatrix} = \begin{pmatrix} e^{-i(k_{n-1}-k_n)z_n} & r_n e^{-i(k_{n-1}+k_n)z_n} \\ r_n e^{i(k_{n-1}+k_n)z_n} & e^{i(k_{n-1}-k_n)z_n} \end{pmatrix} \begin{pmatrix} T_{n,n+1} \\ R_{n,n+1} \end{pmatrix}$$

where $r_n = \frac{k_{n-1}-k_n}{k_{n-1}+k_n}$ is the Fresnel reflection function through the z_n interface separating the ρ_{n-1} and ρ_n SLD's. The solution to the scattering problem is given by noting that beyond the last interface, (i.e., in the bulk), there is a transmitted wave only for which an arbitrary amplitude of the form $\begin{pmatrix} 1 \\ 0 \end{pmatrix}$ can be assumed (i.e., the reflectivity is normalized to the incident beam anyway). The effect of all interfaces is calculated as follows

$$\begin{pmatrix} T_{0,1} \\ R_{0,1} \end{pmatrix} = (M_1) (M_2) \dots (M_n) \dots (M_{N+1}) \begin{pmatrix} 1 \\ 0 \end{pmatrix}$$

with $r_{N+1} = \frac{k_N-k_s}{k_N+k_s}$ in the M_{N+1} matrix given in terms of the substrate k_s . The reflectivity is then given by the ratio

$$R(Q_z) = \left| \frac{R_{0,1}}{T_{0,1}} \right|^2 \quad (22)$$

Applying this procedure to the one *box model* of thickness d with two interfaces yields

$$R(Q_z \equiv 2k_s) = \left| \frac{r_1 + r_2 e^{i2k_s d}}{1 + r_1 r_2 e^{i2k_s d}} \right|^2 \quad (23)$$

Figure 5 shows the calculated reflectivities from a flat liquid interface with two kinds of films (one *box*) of the same thickness d but with different scattering length densities, ρ_1 and ρ_2 . The reflectivities are almost indistinguishable when the normalized SLD's (ρ_i/ρ_s) of the films are complementary to one ($\rho_1/\rho_s + \rho_2/\rho_s = 1$), except for a very minute difference near the first minimum. In the kinematical method described below, the two potentials shown in Fig. 5 yield identical reflectivities.

The matrix method can be used to calculate the exact solution from a finite number of interfaces, and it is most powerful when used with computers by slicing any continuous scattering length density into a histogram. The criteria for determining the optimum number of slices to use is based on the convergence of the calculated reflectivity at a point where slicing the SLD into more boxes does not change the calculated reflectivity significantly.

2b. The Kinematical Approach

The kinematical approach for calculating the reflectivity is only applicable under certain conditions where multiple scattering is not important. It usually fails in calculating the reflectivity at very small angles (or small momentum transfers) near the critical angle. The kinematical approach, also known as the Born-Approximation, gives physical insight in the formulation of $R(Q_z)$ by relating the Fresnel normalized reflectivity, R/R_F , to the Fourier transform of *spatial changes* in $\rho(z)$ across the interface [2] as discussed below.

As in the dynamical approach, $\rho(z)$ is sliced so that $k(z) = \sqrt{k_{z,0}^2 - k_c^2}$ and the reflectance across an arbitrary point z is given by

$$r(z) = \frac{k(z + \Delta z) - k(z)}{k(z + \Delta z) + k(z)} \approx -\frac{4\pi}{4k(z)^2} \frac{d\rho}{dz} dz \approx (Q_c/2Q_z)^2 \frac{1}{\rho_s} \frac{d\rho}{dz} dz \quad (24)$$

In the last step of the derivation, $r(z)$ was multiplied and divided by ρ_s , the SLD of the subphase, and the identity $Q_c^2 \equiv 16\pi\rho_s$ was used. Assuming no multiple scattering, the reflectivity is calculated by integrating over all reflectances at each point, z , with a phase factor $e^{iQ_z z}$ as follows,

$$R(Q_z) = R_F(Q_z) \left| \frac{1}{\rho_s} \int \left(\frac{d\rho}{dz} \right) e^{iQ_z z} dz \right|^2 = R_F(Q_z) |\Phi(Q_z)|^2 \quad (25)$$

where $\Phi(Q_z)$ can be regarded as the *generalized structure factor* of the interface, analogous to the structure factor of a unit cell in 3D crystals. This formula can be also derived by using the Born Approximation, as is shown in the following section.

As an example of the use of Eq. 25 we assume that the SLD at a liquid interface can be approximated by a sum of error functions as follows

$$\rho(z) = \rho_0 + \sum_{j=1}^N \frac{(\rho_j - \rho_{j-1})}{2} \left[1 + \operatorname{erf} \left(\frac{z - z_j}{\sqrt{2}\sigma_j} \right) \right] \quad (26)$$

where ρ_0 is the SLD of the vapor phase and $\rho_N = \rho_s$. Using Eq. 25 the reflectivity is given by

$$R(Q_z) = R_F(Q_z) \left| \sum_j \left(\frac{\rho_j - \rho_{j-1}}{\rho_s} \right) \exp^{-\frac{(Q_z \sigma_j)^2}{2}} \exp^{iQ_z z_j} \right|^2. \quad (27)$$

Assuming one interface at $z_1 = 0$ with surface roughness $\sigma_1 = \sigma$, the Fresnel reflectivity, $R_F(Q_z)$, is simply modified by a Debye-Waller-like factor

$$R(Q_z) = R_F(Q_z) \exp^{-(Q_z \sigma)^2}. \quad (28)$$

The effect of surface roughness on the reflectivities from water and from liquid mercury surfaces assuming gaussian smearing of the interfaces, is shown in Figure 3. Braslau et al. [9] have demonstrated that the Gaussian smearing of the interface due to capillary waves in simple liquids is sufficient in modeling the data, and that more complicated models cannot be supported by the X-ray data.

Applying Eq. 27 to the one box model discussed above (See Fig. 5), and assuming conformal roughness, $\sigma_j = \sigma$, the calculated reflectivity in terms of SLD normalized to ρ_s is

$$R(Q_z) = R_F(Q_z) \left[(1 - \rho_1)^2 + \rho_1^2 + 2\rho_1(1 - \rho_1) \cos(Q_z d) \right] \exp^{-(Q_z \sigma)^2}. \quad (29)$$

In this approximation the roles of the normalized SLD of the one box, ρ_1 , and that for the *complementary* model $\rho_2 = 1 - \rho_1$ are equivalent and demonstrates that the reflectivities for both models are *mathematically* identical. This is the simplest of many examples where two or more distinct SLD models yield identical reflectivities in the Born Approximation. When using the kinematical approximation to invert the reflectivity to SLD there is always a problem of facing a non-unique result. Ways to distinguish between such models is discussed in the Data Analysis section.

In some instances, the scattering length density can be generated by several step functions that are smeared with one gaussian (*conformal roughness* $\sigma_j = \sigma$), representing different moieties of the molecules on the surface. The reflectivity can be calculated by using a combination of the *dynamical* and the *kinematical* approaches [2]. First, the exact reflectivity from the step-like functions ($\sigma = 0$) is calculated using the matrix method, $R_{dyn}(Q_z)$, and the effect of surface roughness is incorporated by multiplying the calculated reflectivity with a Debye-Waller-like factor as follows [2]

$$R(Q_z) = R_{dyn}(Q_z) \exp^{-(Q_z \sigma)^2}. \quad (30)$$

B. Non-specular scattering

The geometry for non-specular reflection is shown in Figure 1(b). The scattering from a 2D system is very weak and enhancements due to multiple scattering processes at the interface is taken advantage of. As is shown in Figure 1(b) the momentum transfer \mathbf{Q} has a finite component parallel to the liquid surface ($\mathbf{Q}_\perp \equiv \mathbf{k}_\perp^i - \mathbf{k}_\perp^f$) enabling determination of lateral correlations in the 2D plane. Exact calculation of scattering from surfaces is practically impossible except for special cases, and the Born Approximation (BA) [47] is usually applied. When the incident beam or the scattered beam are at grazing angles (i.e., near the critical angle), multiple scattering effects modify the scattering and these can be accounted for by a higher order approximation known as the Distorted Wave Born Approximation (DWBA). The features due to multiple scattering at grazing angles provide evidence that the scattering processes indeed occur at the interface.

1. The Born Approximation

In the BA for a general potential $V(\mathbf{r})$ the scattering length amplitude is calculated as follows [47],

$$F(\mathbf{Q}) = \frac{1}{4\pi} \int V(\mathbf{r}) e^{i\mathbf{Q}\cdot\mathbf{r}} d^3\mathbf{r}. \quad (31)$$

where in the present case, $V(\mathbf{r}) = 4\pi\rho(\mathbf{r})$. From the scattering length amplitude the differential cross section is calculated as follows [47]

$$\begin{aligned} \frac{d\sigma}{d\Omega} &= |F(\mathbf{Q})|^2 \\ &= \int [\rho(\mathbf{0})\rho(\mathbf{r})] e^{i\mathbf{Q}\cdot\mathbf{r}} d^3\mathbf{r}. \end{aligned} \quad (32)$$

where $[\rho(\mathbf{0})\rho(\mathbf{r})] \equiv \int [\rho(\mathbf{r}' - \mathbf{r})\rho(\mathbf{r}')] d^3\mathbf{r}'$ is the density-density correlation function. The measured reflectivity is a convolution of the differential cross-section with the instrumental resolution, as discussed below and in the literature [47,9,49].

The scattering length density, ρ , for a liquid-gas interface can be described as a function of the actual height of the surface, $z(x, y)$, as follows,

$$\rho(\boldsymbol{\mu}, z) = \begin{cases} \rho_s & \text{for } z < z(\boldsymbol{\mu}) \\ 0 & \text{for } z > z(\boldsymbol{\mu}) \end{cases} \quad (33)$$

where $\boldsymbol{\mu} = (x, y, 0)$ is a 2D in-plane vector. The height of the interface z is also time dependent and temperature dependent due to capillary waves, and therefore thermal averages of z are used [10,14]. Inserting the SLD Eq. 33, in Eq. 32 and performing the integration over the z coordinate yields

$$F(\mathbf{Q}_\perp, Q_z) = \frac{\rho_s}{iQ_z} \int e^{i[\mathbf{Q}_\perp \cdot \boldsymbol{\mu} + Q_z z(\boldsymbol{\mu})]} d^2\boldsymbol{\mu} \quad (34)$$

where $\mathbf{Q}_\perp = (Q_x, Q_y, 0)$ is an in-plane scattering vector. This formula properly predicts the reflectivity from an ideally flat surface, $z(x, y) = 0$ within the kinematical approximation

$$F(\mathbf{Q}_\perp, Q_z) = \frac{4\pi^2 \rho_s}{iQ_z} \delta^2(\mathbf{Q}_\perp) \quad (35)$$

with a 2D δ function that guarantees specular reflectivity only. The differential cross-section is then given by

$$\frac{d\sigma}{d\Omega} = \pi^2 \left(\frac{Q_c^2}{4Q_z} \right)^2 \quad (36)$$

where $Q_c^2 \equiv 16\pi\rho_s$. This is the general form for the Fresnel reflectivity in terms of the differential cross-section $d\sigma/d\Omega$, which is defined in terms of the flux of the incident beam on the surface. In reflectivity measurements however, the scattered intensity is normalized to the intensity of the incident beam and therefore the flux on the sample is angle dependent

and is proportional to $\sin \alpha_i$. In addition the scattered intensity is integrated over the polar angles α_f and 2θ with $k_0^2 \sin \alpha_i d\alpha_i d(2\theta) = dQ_x dQ_y$, correcting for the flux and integrating

$$R_F(Q_z) \approx \sigma_{tot}(Q_z) = \int \int \left(\frac{d\sigma}{d\Omega} \right) \frac{dQ_x dQ_y}{4\pi^2 k_0^2 \sin \alpha_i \sin \alpha_f} = \left(\frac{Q_c}{2Q_z} \right)^4 \quad (37)$$

as approximated from the exact solution, given in Eq. 17.

Taking advantage of the geometrical considerations above, the differential cross-section to the reflectivity measurement can be readily derived in the more general case of scattering length density that varies along z only, (i.e., $\rho(z)$). In this case, Eqs. 31 can be written as

$$\frac{d\sigma}{d\Omega} = 4\pi^2 \delta^2(\mathbf{Q}_\perp) \left| \int \rho(z) e^{iQ_z z} dz \right|^2 \quad (38)$$

If we normalize $\rho(z)$ to the scattering length density of the substrate, ρ_s , and use a standard identity between the Fourier transform of a function and its derivative, we obtain,

$$\frac{d\sigma}{d\Omega} = \pi^2 \left(\frac{Q_c^2}{4Q_z} \right)^2 \left| \int \frac{1}{\rho_s} \frac{d\rho(z)}{dz} e^{iQ_z z} dz \right|^2 \quad (39)$$

which with the geometrical corrections yields Eq. 25.

Thermal averages of the scattering length density under the influence of capillary waves and the assumption that the SLD of the gas phase is zero can be approximated as follows [10,14],

$$[\rho(\mathbf{0})\rho(\mathbf{r})] \sim \frac{\rho_s}{2} \left(1 + \text{erf} \left[\frac{z}{\sqrt{2}\sigma(\boldsymbol{\mu})} \right] \right) \quad (40)$$

where $\sigma(\boldsymbol{\mu})$ is the height-height correlation function.

Inserting Eq. 40 into Eq. 32 and integrating over z , results in the differential cross-section

$$\frac{d\sigma}{d\Omega} = \frac{2\pi}{Q_z^2} \int e^{i\mathbf{Q}_\perp \cdot \boldsymbol{\mu} - Q_z^2 \sigma^2(\boldsymbol{\mu})} d^2 \boldsymbol{\mu}. \quad (41)$$

and assuming isotropic correlation function in the plane yields [49]

$$\frac{d\sigma}{d\Omega} = \frac{2\pi}{Q_z^2} \int \mu J_0(Q_\perp \mu) e^{-Q_z^2 \sigma^2(\mu)} d\mu \quad (42)$$

where J_0 is a Bessel function of the first kind. This expression was used by Sinha et al. to calculate the diffuse scattering from rough liquid surfaces with a height-height density correlation function that diverges logarithmically due to capillary waves [49,45].

2. Distorted Wave Born-Approximation (DWBA)

Due to the weak interaction of the electromagnetic field (X-rays) with matter (electrons), the BA is a sufficient approach to the scattering from most surfaces. However, as we have already encountered with the reflectivity, the BA fails (or is invalid) when either the incident

beam or the scattered beam is near the critical angle, where multiple scattering processes take place. The effect of the bulk on the scattering from the surface can be accounted for by defining the scattering length density as a superposition of two parts as follows

$$\rho(\mathbf{r}) = \rho_1(z) + \rho_2(\boldsymbol{\mu}, z). \quad (43)$$

Here $\rho_1(z)$ is a step function that defines an ideally sharp interface separating the liquid and gas phases at $z = 0$, whereas the second term, $\rho_2(\boldsymbol{\mu}, z)$, is a quasi two-dimensional function in the sense that it has a characteristic average *thickness* d_c such that $\lim_{z \rightarrow \pm d_c/2} \rho_2(\boldsymbol{\mu}, z) = 0$. It can be thought of as *film*-like and is a detailed function with features that relate to molecular or atomic distributions at the interface. Although the definition of ρ_2 may depend on the location of the interface, ($z = 0$) in ρ_1 , the resulting calculated scattering must be invariant for equivalent descriptions of $\rho(\mathbf{r})$. In some cases ρ_2 can be defined as either a totally external or totally internal function with respect to the liquid bulk, (i.e., ρ_1). In other cases, especially when dealing with liquid surfaces, it is more convenient to locate the interface at some intermediate point coinciding with the center of *mass* of ρ_2 with respect to z . The effect of the substrate term $\rho_1(z)$ on the scattering from ρ_2 can be treated within the distorted wave Born approximation (DWBA) by using the exact solution from the ideally flat interface (Sec. II) to generate the Green function for a higher order Born approximation [47,42,57,49]. The Green function in the presence of an ideally flat interface, ρ_1 , replaces the *free* particle Green function that is commonly used in the Born approximation. The scattering amplitude in this case is given by [47,42]

$$F_{DWBA}(\mathbf{Q}) = F_F(Q_z) + F_2(\mathbf{Q}) = -i\pi Q_z r_F(Q_z) + \int \tilde{\chi}_{\mathbf{k}'}^*(\mathbf{r}) \rho_2(\mathbf{r}) \chi_{\mathbf{k}}(\mathbf{r}) d\mathbf{r} \quad (44)$$

where the exact Fresnel amplitude $F_F(Q_z)$ is written in the form of a scattering amplitude so that Eq. 44 reproduces the Fresnel reflectivity in the absence of ρ_2 .

The exact solution of the step function ρ_1 , $\chi_{\mathbf{k}}(\mathbf{r})$, is given by

$$\chi_{\mathbf{k}}(\mathbf{r}) = e^{i\mathbf{k}_{\perp}^i \cdot \boldsymbol{\mu}} \begin{cases} e^{ik_{z,0}^i z} + r^i(k_{z,s}^i) e^{-ik_{z,s}^i z} & \text{for } z > 0 \\ t^i(k_{z,s}^i) e^{ik_{z,s}^i z} & \text{for } z < 0 \end{cases} \quad (45)$$

and the $\tilde{\chi}_{\mathbf{k}}^*(\mathbf{r})$ is the time reversed and complex conjugate solution of an incident beam with $-\mathbf{k}_i$,

$$\tilde{\chi}_{\mathbf{k}}^*(\mathbf{r}) = e^{-i\mathbf{k}_{\perp}^f \cdot \boldsymbol{\mu}} \begin{cases} t^f(k_{z,0}^f) e^{-ik_{z,0}^f z} & \text{for } z > 0 \\ e^{-ik_{z,s}^f z} + r^f(k_{z,0}^f) e^{ik_{z,0}^f z} & \text{for } z < 0. \end{cases} \quad (46)$$

In the absence of ρ_1 , Eq. 44 transforms into the standard Born Approximation for ρ_2 and this reproduces Eq. 31. The notation for transmission and reflection functions indicate scattering of the wave from the air onto the subphase and *vice-versa* according to $k_{z,s}^i = \sqrt{(k_{z,0}^i)^2 - k_c^2}$, and $k_{z,0}^f = \sqrt{(k_{z,s}^f)^2 + k_c^2}$ respectively. In the latter case, total reflectivity does not occur except for the trivial case $k_{z,s}^f = 0$, and no enhancement due to the evanescent wave is expected. In this approximation, the final momentum transfer in the Q_z direction is a superposition of momentum transfers from ρ_2 (the *film*) and from the liquid interface, ρ_1 . For instance, there could be a wave scattered with $Q_z = 0$ with respect to ρ_2 but reflected

from the surface with a finite Q_z . Assuming that the scattering from the *film* is as strong for Q_z as for $-Q_z$ (as is the case for an ideal 2D system with equal scattering along the rod, i.e., ρ_2 is symmetrical under the inversion of z), we can write $\tilde{\rho}_2(\mathbf{Q}_\perp, Q_z) \approx \tilde{\rho}_2(\mathbf{Q}_\perp, -Q_z)$. It can be shown that the cross-section can be approximated as follows [57,15,49]

$$\frac{d\sigma}{d\Omega} \approx \begin{cases} \left| t^i(k_{z,s}^i) \tilde{\rho}_2(\mathbf{Q}_\perp, Q'_z) t^f(k_{z,s}^f) \right|^2 & \text{for } z > 0 \\ \left| t^i(k_{z,s}^i) \tilde{\rho}_2(\mathbf{Q}_\perp, Q''_z) t^f(k_{z,0}^f) \right|^2 & \text{for } z < 0 \end{cases} \quad (47)$$

where $\mathbf{Q}_\perp \equiv \mathbf{k}_\perp^i - \mathbf{k}_\perp^f$ and $Q'_z = k_{z,0}^i - k_{z,s}^f$ and $Q''_z = k_{z,s}^i - k_{z,0}^f$. Notice that the transmission functions modulate the scattering from the *film* (ρ_2), and in particular they give rise to enhancements as $k_{z,s}^i$ and $k_{z,s}^f$ are scanned around the critical angle as depicted in Figure 2(b). Also, it is only by virtue of the z symmetry of the scatterer that such enhancements occur for an exterior film. From this analysis we notice that there will be no enhancement due to the transmission function of the final wave for an interior *film*.

To examine the results from the DWBA method, we consider scattering from a single scatterer near the surface. The discussion is restricted to that where the detection of the scattered beam is performed in the vapor phase only. The scatterer can be placed either in the vacuum ($z > 0$) or in the liquid (see Fig. 6). When the particle is placed in the vacuum there are two major relevant incident waves: a direct one from the source, labeled 1^i in Figure 6(a); and a second one reflected from the surface before scattering from ρ_2 , labeled 2^i . Assuming inversion symmetry along z , both waves scatter into a finite \mathbf{Q}_\perp with similar strengths at Q_z and $-Q_z$, giving rise to an enhancement near the critical angle if the incident beam is near the critical angle. Another multiple scattering process that gives rise to enhancement at the critical angle is one in which beam 1^i does not undergo a change in the momentum transfer along ($z \ Q_z^{film} \approx 0$) before scattering from the liquid interface. The effect of these processes gives rise to enhancements if either the incident beam or the reflected beam are scanned along the z direction. Slight modifications of the momentum transfer along the z direction (such as $Q'_z = k_z^i + \sqrt{(k_z^i)^2 - k_c^2}$ are neglected in the discussion above). The effective amplitude from the scatterer outside the medium is given by the following terms

$$[e^{iQ_z z} + e^{iQ'_z z} r(k_{z,s}^f)] \approx t(k_{z,s}^i) \quad (48)$$

where the approximation is valid since at small momentum transfers the phase factor can be neglected, and $1 + r(k_{z,s}) = t(k_{z,s})$. At large angles the reflectivity is negligible and the transmission function approaches $t(k_{z,s}) \approx 1$. Similar arguments hold for the outgoing wave. Neglecting the small changes in the momentum transfer due to dynamical effects, the transmission function modulates the scattering as is shown in solid line in Fig. 2(b).

The scattered wave from a particle that is embedded in the medium is different due to the asymmetry between external and internal reflection from the liquid subphase. The wave scattered from the particle re-scatters from the liquid-gas interface. Upon traversing the liquid interface the index of refraction increases from $n = 1 - \delta$ ($\delta = (2\pi/k_0^2)\rho$) to 1 and no total internal reflection occurs as discussed earlier; thus there is no evanescent wave in the medium. The transmission function for this wave is given by $t(-k_{z,s}^i)$, like that of a wave emanating from the liquid interface into the vapor phase. In this case, the transmission function is a real function for all $k_{z,s}^i$ and does not have the enhancements around the critical angle (as shown in Figure 6(b)), with zero intensity at the horizon.

3. Grazing Incidence Diffraction (GID), and Rod Scans

In some instances ordering of molecules at liquid interfaces occurs. Langmuir monolayers spread at the gas-water interface usually order homogeneously at high enough lateral pressures. [22,13,24]. Surface crystallization of n-alkane molecules on molten alkane has been observed recently [58,34]. In these cases, ρ_2 is a periodic function in x and y , and can be expanded as a Fourier series in terms of the 2D reciprocal lattice vectors $\boldsymbol{\tau}_\perp$ as follows

$$\rho_2(\boldsymbol{\mu}, z) = \sum_{\boldsymbol{\tau}_\perp} F(\boldsymbol{\tau}_\perp, z) e^{i\boldsymbol{\tau}_\perp \cdot \boldsymbol{\mu}} \quad (49)$$

Inserting Eq. 49 in Eq. 47 and integrating yields the cross-section for quasi-2D Bragg reflection at $\mathbf{Q}_\perp = \boldsymbol{\tau}_\perp$

$$\frac{d\sigma}{d\Omega} \sim P(\mathbf{Q}) \left| t(k_{z,s}^i) \right|^2 \left\langle |F(\boldsymbol{\tau}_\perp, Q_z)|^2 \right\rangle DW(Q_\perp, Q_z) \left| t^f(k_{z,s}^f) \right|^2 \delta(\mathbf{Q} - \boldsymbol{\tau}_\perp) \quad (50)$$

where $P(\mathbf{Q})$ is a polarization correction, and the 2D unit cell structure factor is given as a sum over the atomic form factors $f_j(Q)$ with appropriate phase

$$F(\boldsymbol{\tau}_\perp, Q_z) = \sum_j f_j(Q) e^{i\boldsymbol{\tau}_\perp \cdot \mathbf{r}_j + Q_z z_j}. \quad (51)$$

The structure factor squared is averaged for multiplicity due to domains and weighted for orientation relative to the surface normal. The ordering of monolayers at the air-water interface is usually in the form of 2D *powder* consisting of crystals with random orientation in the plane. From Eq. 50 we notice that the conservation of momentum expressed with the δ function allows for observation of the Bragg reflection at any Q_z . A rod scan can be performed by varying either the incident or reflected beam, or both. The variation of each will produce some modulation due to both the transmission functions and to the average molecular structure factor along the z -axis. The Debye-Waller factor, $DW(\mathbf{Q}_\perp, Q_z)$, which is due to the vibration of molecules about their own equilibrium position with time dependent molecular displacement $\mathbf{u}(t)$ is given by

$$DW(\mathbf{Q}_\perp, Q_z) \sim e^{-(C_\perp \mathbf{Q}_\perp^2 \langle u_\perp^2 \rangle + Q_z^2 \sigma^2)} \quad (52)$$

The term due to capillary waves on the liquid surface is much more dominant than the contribution from the in-plane intrinsic fluctuations. The Debye-Waller factor in this case is an average over a crystalline size and might not reflect surface roughness extracted from reflectivity measurements, where it is averaged over the whole sample.

III. EXPERIMENTAL CONSIDERATIONS AND DATA ANALYSIS

The minute sizes of interfacial samples on the sub-microgram level combined with the weak interaction of X-rays with matter result in very weak GID and reflectivity (at large Q_z) signals that require highly intense incident beams, which are available at X-ray synchrotron sources. A well prepared incident beam for reflectivity experiments at a synchrotron (for example, the X22B beam-line at the National Synchrotron Light Source at Brookhaven

National Laboratory) has an intensity of $10^9 - 10^{10}$ photons/second, whereas for a similar resolution, an 18 kW rotating anode generator produces $10^4 - 10^5$ photons/second. Although reflectivity measurements can be carried out with standard X-ray generators, the measurements are limited to almost half the angular range accessible at synchrotron sources and they take hours to complete compared to minutes at the synchrotron. GID experiments are practically impossible with X-ray generators since the expected signals (2D-Bragg reflections, for example) normalized to the incident beam are on the order of $10^{-8} - 10^{-10}$.

A. Reflectivity

X-ray reflectivity and GID measurements of liquid surfaces are carried out on special reflectometers that enable manipulation of the incident as well as the outgoing beam. A prototype liquid surface reflectometer was introduced for the first time by Als-Nielsen and Pershan [1]. In order to bring the beam to an angle of incidence α_i with respect to the liquid surface, the monochromator is tilted by an angle χ either about the axis of the incident beam (indicated by χ_1 in Fig. 7) or about the axis normal to the reciprocal lattice wave vector of the monochromator, τ_0 (χ_2). Figure 7 shows the geometry that is used to deflect the beam from the horizon onto the liquid surface at an angle α_i by tilting the monochromator. At the Bragg condition, the surface of the monochromator crystal, is at an angle ψ with respect to the incoming beam. Tilting over the incident beam axis is like tracing the Bragg reflection on the Debye-Scherer cone so that the ψ axis remains fixed, with a constant wavelength at different tilting angles. The rotated reciprocal lattice vector and the final wave-vector in this frame are given by

$$\begin{aligned}\tau_0 &= \tau_0(-\sin \psi, \cos \psi \cos \chi_1, \cos \psi \sin \chi_1) \\ \mathbf{k}_f &= k_0(\cos \alpha_i \cos \phi, \cos \alpha_i \sin \phi, \sin \alpha_i)\end{aligned}\quad (53)$$

where ϕ is the horizontal scattering angle. The Bragg conditions for scattering are given by,

$$\mathbf{k}_i + \tau_0 = \mathbf{k}_f; \quad |\mathbf{k}_f| = k_0 \quad (54)$$

Using Eqs. 53 and 54 the following relations for the monochromator axes are obtained,

$$\begin{aligned}\sin \psi &= \frac{\tau_0}{2k_0} \\ \sin \chi_1 &= \frac{k_0}{\tau_0} \cos \psi \sin \alpha_i \\ \cos \phi &= \left(1 - \frac{\tau_0^2}{2k_0^2}\right) / \cos \alpha_i\end{aligned}\quad (55)$$

And we notice that the monochromator angle ψ is independent of α_i . However, the scattering angle ϕ has to be modified as α_i is varied. This means that the whole reflectometer arm has to be rotated. Similarly, for the configuration where the monochromator is tilted over the axis normal to τ_0 we get

$$\begin{aligned}
\sin \psi &= \frac{\tau_0}{2k_0 \cos \chi_2} \\
\sin \chi_2 &= \frac{k_0}{\tau_0} \sin \alpha_i \\
\cos \phi &= \left(1 - \frac{\tau_0^2}{2k_0^2}\right) / \cos \alpha_i.
\end{aligned} \tag{56}$$

From these relations the conditions for a constant wavelength operation for any angle of incidence, α_i , can be calculated and applied to the reflectometer. Here, unlike the previous mode, deflection of the beam to different angles of incidence requires both, the adjustment of ψ as well as ϕ in order to maintain a constant wavelength. If ψ is not corrected in this mode of operation, the wavelength varies as χ is varied. This mode is sometimes desirable, especially when the incident beam hitting the monochromator consists of a continuous distribution of wavelengths around the wavelength at horizontal scattering, $\chi_2 = 0$. Such continuous wavelength distribution exists when operating with X-ray tubes, or when the tilting monochromator is facing the *white* beam of a synchrotron. Although, the variation in the wavelength is negligible as χ_2 is varied, without the correction of ψ , the exact wavelength and the momentum transfer can be computed using the relations in Eq. 57. In both modes of monochromator tilting, the surface height as well as the height of the slits are adjusted with vertical translations.

The exact angle of the monochromatic incident beam on the surface is determined by at least two *horizontal* slits located between the sample and the source. One of these slits is usually located as close as possible to the sample, and the other as close as possible to the source. These two slits determine the resolution of the incident beam. By deflecting the beam from the horizon the shape of the beam changes and that may change incident beam intensity going through the slits, and the use of a monitor right after the slit in front of the sample is essential for the absolute determination of the reflectivity. The size of the two slits defining the incident beam, is chosen in such a way that the foot-print of the beam is much smaller than the width of the reflecting surface so that total reflectivity occurs. Figure 8 shows the reflected beam and the direct beam from a flat surface of water demonstrating total reflectivity at $Q_z = 0.85Q_c$. In this experiment the detector slit is wide open at about ten times the opening of the sample slit. As is demonstrated, the effect of absorption is negligible for water, and roughness is significantly reduced by damping surface waves. The damping can be achieved by reducing the height of the water film to about $\approx 0.3\text{mm}$ and placing a passive as well as an active anti-vibration unit underneath the liquid sample holder, suppressing mechanical vibrations [24].

B. Non-specular Scattering - GID, Diffuse Scattering and Rod Scans

X-ray GID measurements are performed at angles of incidence below the critical angle $\approx 0.9\alpha_c$. Operating with the incident beam below the critical angle enhances the signal from the surface with respect to that of the bulk, by creating an evanescent wave in the medium that is exponentially decaying as,

$$E(z) = t(k_{z,s})e^{-z/\Lambda} \tag{57}$$

where

$$\frac{1}{\Lambda} = \sqrt{k_c^2 - k_{z,0}^2}. \quad (58)$$

For water at $k_z \approx 0.9k_c$, $\Lambda \sim 1000 \text{ \AA}$.

As illustrated in Figure 1(b), the components of the momentum transfer for GID are given by,

$$\begin{aligned} Q_z &= k_0(\sin \alpha_i + \sin \alpha_f) \\ Q_x &= k_0(\cos \alpha_i - \cos \alpha_f) \cos 2\theta \\ Q_y &= k_0 \cos \alpha_f \sin 2\theta \end{aligned} \quad (59)$$

In most cases, the 2D order on liquid surfaces is powder like, and the lateral scans are displayed in terms of Q_{\perp} which is given by,

$$Q_{\perp} = k_0 \sqrt{\cos^2 \alpha_i + \cos^2 \alpha_f - 2 \cos \alpha_i \cos \alpha_f \cos 2\theta} \quad (60)$$

To determine the in-plane correlations the horizontal resolution of the diffractometer can be adjusted with a soller collimator that consists of vertical absorbing foils stacked together between the surface and the detector. The area that is probed at each scattering angle 2θ is proportional to $S_0 / \sin 2\theta$, where S_0 is the area probed at $2\theta = \pi/2$. The probed area must be taken into account in the analysis of a GID scan that is performed over a wide range of angles.

Position sensitive detectors (PSD) are commonly used to measure the intensity along the 2D rods. It should be kept in mind that the intensity along the PSD is not a true rod scan of a Bragg reflection at a nominal Q_{\perp} because of the variation in Q_{\perp} as α_f is varied as is seen in Eq. 59.

C. Data Analysis

The task of finding the SLD from a reflectivity curve is similar to that of finding an effective potential for Eq. 7 from the modulus of the wave-function. Direct inversion of the scattering amplitude to SLD is not possible except for special cases when the BA is valid [44]. If the modulus and the phase are known they can be converted by the method of Gelfand-Levitran-Marchenko [44] to SLD (GLM method). However, in reflectivity experiments the intensity of the scattered beam alone is measured, and phase information is lost.

Direct reconstruction of step-like potentials have been developed recently by retrieving the phase from the modulus i.e., reflectivity and then using the GLM method [44,11]. Model-independent methods which are based on optimization of a model to reflectivity, without the requirement of any knowledge of the chemical composition of the SLD at the interface were also developed recently [37,61]. Such models incorporate a certain degree of objectivity. These methods are based on the kinematical and the dynamical approaches for calculating the reflectivity. One method [37] uses indirect Fourier transformation to calculate the correlation function of $d\rho/dz$ which is subsequently used in a square-root deconvolution model

to construct the SLD model. Zhou and Chen, on the other hand, developed a *groove tracking method* that is based on an optimization algorithm to reconstruct the SLD using the *dynamical* approach to calculate the reflectivity at each step [61].

The most common procedure to extract structural information from reflectivity is by using standard non-linear least squares refinement of an initial SLD model. The initial model is defined in terms of a P -dimensional set of independent parameters, \mathbf{p} , using all the available information in guessing of $\rho(z, \mathbf{p})$. The parameters are then refined by calculating the reflectivity ($R[Q_z^i, \mathbf{p}]$) with the tools described earlier and by minimizing the $\chi^2(p)$ quantity,

$$\chi^2(\mathbf{p}) = \frac{1}{N - P} \sum_{i=1} \left[\frac{R_{exp}(Q_z^i) - R(Q_z^i, \mathbf{p})}{\epsilon(Q_z^i)} \right]^2. \quad (61)$$

where $\epsilon(Q_z^i)$ is the uncertainty of the measured reflectivity, $R_{exp}(Q_z^i)$ and N is the number of measured points. The criteria for a good fit can be found in [4]. Uncertainties of a certain parameter can be obtained by fixing it at various values and for each value refining the rest of the parameters until χ^2 is increased by a factor of at least $1/(N - P)$.

The direct methods and model-independent procedures of reconstruction SLD do not guarantee uniqueness of the potential i.e., there can be multiple SLD profiles that essentially yield the same reflectivity curve, as discussed with regard to Figure 5, for example. The uniqueness can be achieved by introducing physical constraints that are incorporated into the parameters of the model. Volume, in-plane density of electrons etc., are among such constraints that can be used, (applying such constraints is discussed briefly in the Examples section [51,52,18]). These constraints reduce the uncertainties and make the relationship of the SLD to the actual molecular arrangement apparent. In the *dynamical* approach no two potentials yield exactly the same reflectivity although the differences between two models might be too small to be detected in an experiment.

An experimental method to solving such a problem was suggested by Sanyal et al., using anomalous X-ray reflectivity methods. Two reflectivity curves from the same sample are measured with two different X-ray energies, one below and one above an absorption edge of the substrate atoms, thereby varying the scattering length density of the substrate [46]. Subsequently the two reflectivity curves can be used to perform a direct Fourier reconstruction [46] or by refinement methods to remove ambiguities. This method is not efficient when dealing with liquids that consist of light atoms because of the very low energy of the absorption edge with respect to standard X-ray energies. Another way to overcome the problem of uniqueness is by performing reflectivity experiments on similar samples with X-rays and with neutrons. In addition, the SLD, $\rho(z)$ across the interface can be changed significantly, in neutron scattering experiments, by chemical exchange of isotopes that change $\rho(z)$, but maintain the same structure [51]. The reflectivities (X-ray as well as neutrons) can be fitted to one structural model that is defined in terms of geometrical parameters only, calculating the SLD's from scattering lengths of the constituents and the geometrical parameters [51,52].

IV. EXAMPLES

Since the pioneering work of Als-Nielsen and Pershan [1], X-ray reflectivity and GID became standard tools for the characterization of liquid surfaces on the atomic length scales.

The techniques have been exploited in studies of the physical properties of simple liquids [9,45,33], Langmuir monolayers [22,13,23,24,2,51], liquid metals [41,31,40], surface crystallization [58–60,34], liquid crystals [39], surface properties of quantum liquids [30], protein recognition processes at liquid surfaces [53,54,29] and many other applications. Here, only several examples are briefly described in order to demonstrate the strengths and the limitations of the techniques. In presenting the examples, there is no intention of giving a full theoretical background of the systems.

A. Simple Liquids

The term simple liquid is usually used for mono-atomic systems governed by Van der Waals type interactions such as, liquid argon. Here, the term is extended to include all classical dielectric (non-metallic) liquids such as water, solvents (methanol, ethanol, chloroform etc.) and others. One of the main issues regarding dielectric liquids is the determination of the average density profile across the interface, $N(z)$. This density is the result of folding the *intrinsic* density $N_I(z)$ of the interface due molecular size, viscosity, and compressibility of the fluid with density fluctuations due to capillary waves, $\delta N_{CW}(z)$. The continuous nature of the density across the interface due to capillary waves was worked out by Buff, Lovett and Stillinger (BLS) [10] assuming that $N_I(z)$ is an ideal step like function. The probability for the displacement is taken to be proportional to the Boltzmann factor, $e^{-\beta U(z)}$, where U is the free energy necessary to disturb the surface from equilibrium state (i.e., $z(x, y) = 0$), and $\beta = 1/k_B T$. The free energy of an incompressible and non-viscous liquid surface consists of two terms; a surface tension (γ) term, that is proportional to the changes in area from the ideally flat surface and a gravitational term as follows,

$$\begin{aligned} U &= \int \left(\gamma \left[\sqrt{1 + |\nabla z|^2} - 1 \right] + \frac{1}{2} m_s g z^2 \right) d^2 \mu \\ &\approx \frac{1}{2} \int \left(\gamma |\nabla z|^2 + m_s g z^2 \right) d^2 \mu \end{aligned} \quad (62)$$

where m_s is the mass density of the liquid substrate. By using standard Gaussian approximation methods Buff et al find, that $U(z) \sim \frac{z^2}{2\sigma_0^2}$. After convolution of the probability with a step like function, representing the intrinsic density of the liquid surface, yields the following density function,

$$N(z) = N_s \operatorname{erfc} \left(\frac{z}{\sqrt{2}\sigma} \right) \quad (63)$$

with a form similar to the one given in Eq. 40. The average surface roughness at temperature T , is then given by

$$\sigma_{CW}^2 = \frac{k_B T}{2\pi\gamma} \ln \left(\frac{L}{a_0} \right) \quad (64)$$

where a_0 is a molecular diameter and L is the size of the surface. Notice the logarithmic divergence of the fluctuations as the size of the surface increases, as expected of a 2D system [25]. This model was further refined by assuming that the intrinsic profile has a finite width

[14]. In particular if the width due to the intrinsic profile is also expressed by a Gaussian then, the effective surface roughness is given by

$$\sigma_{eff}^2 = \sigma_I^2 + \sigma_{CW}^2 \quad (65)$$

and the calculated reflectivity is similar to Eq. 28 for an interface that is smeared like the error function.

$$R_{CW} = R_F(Q_z) e^{-\sigma_{eff}^2 Q_z^2} \quad (66)$$

Fig. 9 shows the reflectivity from pure water measured at the synchrotron [56] where it is shown that using Eq. 66 for fitting the reflectivity data is satisfactory implying that the error function type of density profile (BLS model) for the liquid interface is sufficient. In the refinement procedure only one parameter, the surface roughness σ , is varied ($\sigma = 2.54 \text{ \AA}$). This small roughness value depends on the attenuation of capillary waves by minimizing the depth of the water to about 0.3mm by placing a flat glass under the water [24]. The validity of gaussian approximation of $N(z)$ (BLS model) was examined by various groups and for a variety of systems [9,45,33]. Ocko et al. have measured the reflectivity of liquid alkanes, over a wide range of temperatures verifying that the surface roughness is of the form given in Eqs. 64and 65 [33].

Experimentally, the reflectivity signal at each Q_z from a rough interface is convoluted with the resolution of the spectrometer in different directions. The effect of the resolution along the Q_z can be calculated analytically or convoluted numerically by computation. For simplicity, we consider that the resolution functions can be approximated as a Gaussian with a width of ΔQ_z along the Q_z can be taken as $e^{-Q_z^2/\Delta Q_z^2}$ with appropriate normalization factor [8]. The resolution, ΔQ_z , is Q_z dependent as the angles of incidence and scattering are varied [33]. However, if we assume that around a certain Q_z the resolution is a constant and we measure σ_{exp} the convolution of the *true* reflectivity with the resolution function yields the following relation,

$$\frac{1}{\sigma_{exp}^2} \approx \frac{1}{\sigma_{eff}^2} + \Delta Q_z^2 \quad (67)$$

from which the *effective roughness* can be extracted as follows,

$$\sigma_{eff} \approx \frac{\sigma_{exp}}{\sqrt{1 - \sigma_{exp}^2 \Delta Q_z^2}} \quad (68)$$

Thus, if the resolution is infinitely *good* i.e., a $\Delta Q_z = 0$ the measured and effective roughness are the same. However, as the resolution is relaxed, the measured roughness gets smaller than the *effective roughness*. The effect of the resolution on the determination of true surface roughness was discussed rigorously by Braslau et al. [9].

Diffuse scattering from liquid surfaces is practically inevitable, due to the presence of capillary waves. Calculation of the scattering from disordered interfaces of various characteristics were treated in [49]. In the Born approximation, true specular scattering from liquid surfaces exist only by virtue of the finite cutoff-length of the mean-square height fluctuations. In other words, the fluctuations due to capillary waves diverge logarithmically and only due to the finite instrumental resolution that true specular reflectivity is observed. The theory for the diffuse scattering from *fractal* surfaces and other rough surfaces was developed in [49].

B. Langmuir Monolayers

A Langmuir monolayer (LM) is a monomolecular amphiphilic film spread at the air-water interface. Each amphiphilic molecule consists of a polar head group (hydrophilic moiety) and a nonpolar tail typically hydrocarbon (hydrophobic) chains [17,50]. Typical examples are fatty acids, lipids, alcohols and others. The length of the hydrocarbon chain can be varied chemically, affecting the hydrophobic character of the molecule. Whereas, the head-group can be ionic, dipolar, or with a certain shape that might attract specific compounds present in the aqueous solution. One important motivation to studying LM's is their close relationship to biological systems. Membranes of all living cells and organelles within cells consist of a lipid bilayers interpenetrated with specific proteins, alcohols, and other organic compounds that combine to give functional macromolecules that determine transport of matter and energy through them. It is well known that biological functions are structural, and structures can be determined by XR and GID. In addition, delicate surface chemistry can be carried out at the head-group interface with molecules from the aqueous solution. From the physics point of view, the LM belongs to an important class of quasi- 2D system with which statistical models that depend on the dimension of the system can be examined.

Herein, results from a simple lipid, dihexadecyl hydrogen phosphate (DHDP), consisting of a phosphate head group (PO_4^-) and two hydrocarbon chains attached to it, are presented. Figure 10(a) displays the normalized reflectivity of a DHDP monolayer at the air-water interface at a lateral pressure of 40 mN/m. The corresponding electron density profile is shown in the inset as a solid line. The profile in the absence of surface roughness ($\sigma = 0$) is displayed as a dashed line. The bulk water subphase corresponds to $z < 0$, the phosphate headgroup region is at $0 \geq z \geq 3.4\text{\AA}$ and the hydrocarbon tails are at the $3.4\text{\AA} \geq z \geq 23.1\text{\AA}$ region. As a first stage analysis of the reflectivity a model SLD with minimum number of *boxes*, $i = 1, 2, 3, \dots$, is constructed. Each box is characterized by a thickness d_i and an electron densities $N_{e,i}$, and one surface roughness, σ for all interfaces. Refinement of the reflectivity with Eq. 30 shows that the two *box* model is sufficient. In order to improve the analysis we can take advantage of information we know of the monolayer i.e., the constituents used and the molecular area determined from the lateral-pressure versus molecular area isotherm. If the monolayer is homogeneous and not necessarily ordered, we can assume an average area per molecule at the interface A , and calculate the electron density of the tail region as follows

$$\rho_{tail} = N_{e,tail}r_0/(Ad_{tail}) \quad (69)$$

where $N_{e,tail}$ is the number of electrons in the hydrocarbon tail and d_{tail} is the length of the tail in the monolayer. The gain in this description is two fold; first, the number of independent parameters can be reduced, and constraints on the total number of electrons can be introduced. However, in this case, the simple relation $\rho_{head} = N_{e,phosphate}/(Ad_{head})$ is not satisfactory and in order to get a reasonable fit *additional* electrons are necessary in the head-group region. These additional electrons can be associated with water molecules that interpenetrate the head group region which is not densely packed. The cross section of the phosphate head group is smaller than the area occupied by the two hydrocarbon tails allowing for water molecules to penetrate the head group region. We therefore introduce an extra parameter N_{H_2O} , the number of water molecules with ten electrons each. The electron density of the head group region is given by,

$$\rho_{head} = (N_{e,phosphate} + 10N_{H_2O})/(Ad_{head}). \quad (70)$$

This approach gives a physical insight into the chemical constituents at the interface. In modeling the reflectivity with the above assumptions we can either apply volume constraints or equivalently examine the consistency of the model with the literature values of closely packed moieties. In this case the following volume constraint can be applied,

$$V_{headgroup} = Ad_{head} = N_{H_2O}V_{H_2O} + V_{phosphate} \quad (71)$$

where $V_{H_2O} \approx 30 \text{ \AA}^2$ is known from the density of water. The value of $V_{phosphate}$ determined from the refinement, should be consistent within error with known values extracted from crystal structures of salt phosphate [18].

Another parameter that can be deduced from the analysis is, the average tilt angle, t , of the tails with respect to the surface from the relation,

$$d_{tail}/l_{tail} = \cos t \quad (72)$$

where l_{tail} is the full length of the extended alkyl chain evaluated from the crystal data for alkanes [18]. Such a relation is valid under the condition that the electron density of the tails when tilted is about the same as that of closely packed hydrocarbon chains in a crystals $\rho_{tail} \approx 0.32e/\text{\AA}^3 r_0$ as observed [23]. Such a tilt of the hydrocarbon tails would lead to an average increase in the molecular area compared to the cross section of the hydrocarbon tails (A_0),

$$A_0/A = \cos t. \quad (73)$$

Gregory et al. found that at lateral pressure, $\pi = 40mN/m$ the average tilt angle is very close to zero ($\approx 7 \pm 7^\circ$) and extract an $A_0 \approx 40.7\text{\AA}^2$ compared with a value of 39.8\AA^2 for closely packed crystalline hydrocarbon chains. The small discrepancy was attributed to defects at domain boundaries.

The GID for the same monolayer is shown in Fig. 10(b) where a lowest order Bragg reflection at 1.516\AA^{-1} is observed. This reflection corresponds to the hexagonal ordering of the individual hydrocarbon chains [22,23] with lattice constant $d = 4.1144\text{\AA}$, and molecular area per chain $A_{chain} = 19.83\text{\AA}^2$. Note that in DHDP the phosphate group is anchored to a pair of hydrocarbon chains with molecular area $A = 39.66\text{\AA}^2$, and it is surprising that ordering of the head group with a larger unit cell (twice that of the hydrocarbon unit cell) is not observed as is evidenced from Fig. 10(b). Also shown in the inset of Fig. 10(b) is a rod scan of the Bragg reflection. To model the rod scan in terms of tilted chains the procedure developed in [23] is followed. The structure factor of the chain can be expressed as

$$F_{chain}(\mathbf{Q}'_\perp, Q'_z) = F(Q_\perp) \frac{\sin(lQ'_z/2)}{(lQ'_z/2)} \quad (74)$$

where $F(Q'_\perp)$ is the in-plane Fourier transform of the cross section of the electron density of chain weighted with the atomic form factors of the constituents. The second term accounts for the length of the chain and is basically a Fourier transform of a one dimensional aperture of length l . If the chains are tilted with respect to the surface normal (in the y-z plane) by an angle t , the \mathbf{Q}' should be rotated as follows,

$$\begin{aligned}
Q'_x &= Q_x \cos t + Q_z \sin t \\
Q'_y &= Q_y \\
Q'_z &= -Q_x \sin t + Q_z \cos t
\end{aligned} \tag{75}$$

For small chain-tilt angles this rotation mainly affects the Q_z dependent part of the chain structure factor, since the Q_{\perp} changes. Applying this transformation to molecular structure factor, Eq. 74, and averaging over all six domains (see more details in Ref. [23] with the appropriate weights to each tilt direction we find that at 40 mN/m the hydrocarbon chains are practically normal to the surface consistent with the analysis of the reflectivity.

In recent Brewster Angle Microscopy (BAM) and X-ray studies of C_{60} -propylamine spread at the air-water interface (see more details on fullerene films [55]), a broad in-plane GID signal was observed [16]. The GID signal was analyzed in terms of a 2D radial distribution function that implied short range positional correlations extending to only few molecular distances. It was demonstrated that the local packing of molecules on water is hexagonal, forming a 2D amorphous solid. This is a detailed study demonstrating how to analyze homogeneously disordered 2D system by combining X-ray scattering techniques and visible light microscopy.

C. Surface Crystallization of Liquid Alkanes

Normal alkanes are linear hydrocarbon chains $(CH_2)_n$ terminating with CH_3 groups similar to fatty acids and lipids that by contrast posses a hydrophilic head groups at one end. Recent extensive X-ray studies of pure and mixed liquid alkanes [58–60,34] reveal a rich and remarkable properties near their melting temperature, T_f . In particular, a single crystal monolayer is formed at the surface of an isotropic liquid bulk up to $\approx 3^\circ C$ above T_f for a range of hydrocarbon number n . The surface freezing phenomena exists for a wide range of chain lengths $16 \geq n \geq 50$. The molecules in the ordered layer are hexagonally packed and show three distinct ordered phases: two rotator phases, one with the molecules oriented vertically ($16 \geq n \geq 30$) and the other tilted toward nearest neighbors. ($30 \geq n \geq 44$). The third phase ($44 \geq n$) orders with the molecules tilted towards next-nearest neighbors. In addition to the 2D Bragg reflections observed in the GID studies, reflectivity curves from the same monolayers were found to be consistent with a one *box* model of densely packed hydrocarbon chains, and a thickness that corresponds to slightly tilted chains. This is an excellent demonstration where no other technique but the X-ray experiments carried out at a synchrotron could be applied to get the detailed structure of the monolayers. Neutron scattering from this system would have yielded similar information, however the intensities available today from reactors and spallation sources are smaller by at least a factor of 10^5 counts/sec for similar resolutions and will not allow observation of any GID signals above background levels.

D. Liquid Metals

Liquid metals unlike dielectric liquids consist of the classical *ionic* liquid and quantum free electron gas. Scattering of conduction electrons at a step like potential (representing the

metal-vacuum interface), give rise to quantum interference effects and lead to oscillations of the electron density across the interface [26]. This effect is similar to the Friedel oscillations in the screened potential arising from the scattering of conduction electrons by an isolated charge in a metal. By virtue of their mobility, the ions in a liquid metal can in turn rearrange and conform to these oscillations to form layers at the interface, not necessarily commensurate with the conduction electron density [41]. Such theoretical predictions of atomic layering at surfaces of liquid metals were known for a long time and were only recently confirmed by X-ray reflectivity studies for liquid gallium and liquid mercury [31,40]. X-ray reflectivities of these liquids were extended to $Q_z \sim 3\text{\AA}^{-1}$ showing a single peak that indicates layering with spacing on the order of atomic diameters. The exponential decay for layer penetration into the bulk of Ga (6.5\AA) was found to be larger than that of Hg ($\sim 3\text{\AA}$). Figure 11 shows a peak in the reflectivity of liquid Ga under *in situ* UHV oxygen free surface cleaning [40]. The normalized reflectivity was fitted to a model scattering length density shown in Figure 11(b) of the following oscillating and exponentially decaying form [40],

$$\rho(z)/\rho_s = \text{erf}[(z - z_0)/\sigma] + \theta(z)A \sin(2\pi z/d)e^{-z/\xi} \quad (76)$$

where $\theta(z)$ is a step function, d is the inter-layer spacing, ξ the exponential decay length, and A an amplitude. Fits to this model are shown in Fig. 11 with $d = 2.56\text{\AA}$, $\xi = 5.8\text{\AA}$. The layering phenomena in Ga showed a strong temperature dependence. Although liquid Hg exhibits layering with a different decay length the reflectivity at small momentum transfers, Q_z are significantly different than that of liquid Ga indicating fundamental differences in the surface structures of the two metals. The layering phenomena suggests in-plane correlations that might be different than those of the bulk, but had not been observed yet with GID studies.

ACKNOWLEDGMENTS

The author would like to thank Prof. P. S. Pershan for providing a copy of Fig. 11 for this publication. Ames Laboratory is operated by Iowa State University for the U.S. Department of Energy under Contract No. W-7405-Eng-82. The work at Ames was supported by the Director for Energy Research, Office of Basic Energy Sciences.

APPENDIX A.

p-polarized X-ray beam

A p-polarized X-ray beam has a magnetic field component that is parallel to the stratified medium (along the x-axis, see Fig. 1), and straightforward derivation of the wave equation 7 yields

$$\frac{d}{dz} \left(\frac{dB}{\epsilon dz} \right) + [k_z^2 - V(z)] B = 0. \quad (77)$$

By introducing a dilation variable Z such that, $dZ = \epsilon dz$ Eq. 77 for B can be transformed to a form similar to Eq. 12

$$\frac{d^2B}{dZ^2} + \left[\frac{k_z^2 - V(z)}{\epsilon} \right] B = 0. \quad (78)$$

The solution of Eq. 78 for an ideally flat interface in terms of $r_p(k_{z,s})$ and $t_p(k_{z,s})$ is then simply given by

$$r_p(k_{z,s}) = \frac{k_{z,0} - k_{z,s}/\epsilon}{k_{z,0} + k_{z,s}/\epsilon}, \quad t_p(k_z, s) = \frac{2k_{z,0}}{k_{z,0} + k_{z,s}/\epsilon} \quad (79)$$

The critical momentum transfer for total external reflectivity of the p-type X-ray beam is $Q_c = 2k_c = 4\sqrt{\pi\rho_s}$, identical to the one derived for the s-type wave. Also, for $2k_z^B \gg Q_z \gg Q_c$, (k_z^B is defined below), $R_F(Q_z)$ can be approximated as

$$R_F(Q_z) \sim \left(\frac{Q_c}{2Q_z} \right)^4 \left(\frac{2}{1 + \epsilon} \right)^2. \quad (80)$$

The factor on the right hand side is one for all practical liquids, and thus the Born approximation is basically the same as for the s-polarized X-ray beam (Eq. 17). The main difference between the s-type and p-type waves occurs at larger angles near a Brewster angle that is given by $\theta_B = \sin^{-1}(k_z^B/k_0)$. At this angle, total transmission of the p-type wave occurs ($r_p(k_{z,s}) = 0$). Using Eqs. 14 and 79, k_z^B can be derived,

$$\frac{k_z^B}{k_0} = \frac{1}{\sqrt{2 - 4\pi\rho_s/k_0^2}}. \quad (81)$$

The Brewster angle for X-rays is then given by $\theta_B = \sin^{-1}(k_z^B/k_0) \approx \pi/4$. This derivation is valid for solid surfaces, including crystals, where the total transmission effect of the p-polarized wave at a Bragg reflection is used to produce polarized and monochromatic X-ray beam.

REFERENCES

- [1] Als-Nielsen J., and Pershan, P.S., 1983. Synchrotron X-ray diffraction study of liquid surfaces. *Nucl. Inst. Meth.* 208: 545-548.
- [2] Als-Nielsen. J., and Kjaer, K., 1989. X-ray reflectivity and diffraction studies of liquid surfaces and surfactant monolayers. In *Phase Transitions in Soft Condensed Matter*. T. Riste and D. Sherrington, editors. Plenum Press, New York. 113-138.
- [3] Azzam, R.M.A., and Bashara, N.M., 1977. *Ellipsometry and Polarized Light*, North Holland: New York.
- [4] Bevington, P.R., 1968. *Data Reduction and Error Analysis*, McGraw Hill New York.
- [5] Binnig, G., and Rohrer, H., 1983. Scanning tunneling microscopy. *Surf. Sci.* 126: 236 -244.
- [6] Binnig, G 1992. Force Microscopy. *Ultramicroscopy* 42-44:7-15.
- [7] Born M., and Wolf, E., 1959. *Principles of Optics*, MacMillan, New York.
- [8] Bouwman, W.G., and Pedersen, J.S., 1996. Resolution function for two-axis specular neutron reflectivity. *J. Appl. Crystall.* 28:152-158.
- [9] Braslau, A., Pershan, P.S., Swislow, G., Ocko, B.M., and Als-Nielsen, J., 1988. Capillary waves on the surface of simple liquids measured by X-ray reflectivity. *Phys. Rev. B* 38:2475-2469.
- [10] Buff, F.P., Lovett, R.A., and Stillinger, Jr., F.H., 1965. Interfacial density profile for fluids at the critical region. *Phys. Rev. Lett.* 15:621-623.
- [11] Clinton, W.L., 1993. Phase determination in X-ray and neutron reflectivity using logarithmic dispersion relations. *Phys. Rev. B* 48:1-5.
- [12] Ducharme, D., Max, J.-J., Salesse, C., and Leblanc, R.M., 1990. Ellipsometric study of the physical states of phosphotadylcholines at the air-water interface. *J. Phys. Chem.* 94: 1925-1932.
- [13] Dutta, P., Peng, J.B., Lin, B., Ketterson, J.B., and Prakash, M. P. Georgopoulos, and S. Ehrlich, 1987. X-ray diffraction studies of organic monolayers on the surface of water. *Phys. Rev. Lett.* 58:2228-2231.
- [14] Evans, R., 1979. The Nature of the liquid-vapor interface and other topics in the statistical mechanics of non-uniform, classical fluids. *Advances in Physics* 28:143-200.
- [15] Feidenhas'l, R., 1989. Surface structure determination by X-ray diffraction. *Surface Science Reports* 10:105-188.
- [16] Fukuto, M., Penanen, K., Heilman, R.K., Pershan, P.S., and Vaknin, D., 1997. C₆₀-propylamine adduct monolayers at the gas/water interface: Brewster angle microscopy and x-ray scattering study. *J. Chemical Physics J. Chem. Phys.* 107:5531-5546.
- [17] Gaines, G. 1966. *Insoluble Monolayers at Liquid Gas Interface*. Interscience, New York.
- [18] Gregory, B.W., Vaknin, D., Gray, J.D., Ocko, B.M., Stroeve, P., Cotton, T.M., and Struve, W.S., 1997. Two-dimensional pigment monolayer assemblies for light harvesting applications: Structural Characterization at the air/water interface with X-ray specular reflectivity and on solid substrates by optical absorption spectroscopy. *J. Phys. Chem. B* 101:2006-2019.
- [19] Henon, S., and Meunier, J., 1991. Microscope at the Brewster angle: Direct observation of first-order phase transitions in monolayers. *Rev. Sci. Instrum.* 62:936-939.
- [20] Höning, D., and Möbius, D., 1991. Direct visualization of monolayers at the air-water interface by Brewster Angle Microscopy. *J. Phys. Chem.* 95: 4590-4592.

[21] *International Tables For Crystallography* Volume C, edited by A. J. C. Wilson, Kluwer (1992).

[22] Kjaer, K., Als-Nielsen, J., Helm, C.A., Laxhuber, L.A., and Möhwald, H., 1987. Ordering in lipid monolayers studied by synchrotron x-ray diffraction and fluorescence microscopy. *Phys. Rev. Lett.* 58:2224-2227.

[23] Kjaer, K., Als-Nielsen, J., Helm, C.A., Tippman-Krayer, P., and Möhwald, H., 1989. Synchrotron X-ray diffraction and reflection studies of arachidic acid monolayers at the air-water interface. *J. Phys. Chem.* 93:3202-3206.

[24] Kjaer, K. Als-Nielsen, J., Lahav, M., and Leiserowitz, L., 1994. Two-dimensional crystallography of amphiphilic molecules at the air-water interface. In *Neutron and Synchrotron Radiation for Condensed Matter Studies*, Vol. III, J. Baruchel, J-L Hodeau, M. S. Lehmann, J.-R. Regnard, and C. Schlenker, Editors. Springer-Verlag Berlin Heidelberg. 47-69.

[25] Landau, L.D., and Lifshitz, E.M., 1980. *Statistical Physics*, Pergamon Press, page 435.

[26] Lang N.D., and Kohn, W. 1970. Theory of metal surfaces: Charge density and surface energy. *Phys. Rev. B1*, 4555-4568 (1970).

[27] Lekner, J., 1987. *Theory of Reflection of Electromagnetic Waves and Particles*, Martinus Nijhoff Publishers.

[28] Lösche, M., and Möhwald, H., 1984. Fluorescence microscope to observe dynamical processes in monomolecular layers at the air/water interface. *Rev. Sci. Instrum.* 55:1968-1972.

[29] Lösche, M., Piepenstock, M., Diederich, A., Grünewald, T., Kjaer, K., and Vaknin, D., 1993. Influence of surface chemistry on the structural organization of monomolecular protein layers adsorbed to functionalized aqueous interfaces. *Biophysical J.* 65:2160-2177.

[30] Lurio, L.B., Rabedeau, T.A., Pershan, P.S., Silvera, I.S., Deutsch, M., Kosowsky, S.D., and Ocko, B.M., 1992. Liquid-vapor density profile of Helium: An X-ray study. *Phys. Rev. Lett.* 68:2628-2631.

[31] Magnussen, O.M., Ocko, B.M., Regan, M.J., Penanen, K., Pershan, P.S., and Deutsch, M. 1995. X-ray reflectivity measurements of surface layering in mercury. *Phys. Rev. Lett.* 74 4444-4447.

[32] Möhwald, H., 1990. Phospholipid and phospholipid-protein monolayers at the air/water interface. *Annu. Rev. Phys. Chem.* 41:441-476.

[33] Ocko, B.M., Wu, X.Z., Sirota, E.B., Sinha, S.K., and Deutsch, M., 1994. X-ray reflectivity study of thermal capillary waves on liquid surfaces. *Phys. Rev. Lett.* 72:242-245.

[34] Ocko, B.M., Wu, X.Z., Sirota, E.B., Sinha, S.K., Gang, O., and Deutsch, M., 1997. Surface freezing in chain Molecules: I. Normal-Alkanes. *Phys. Rev. B.* (preprint).

[35] Panofsky, W.K.H., and Phillips, M., 1962. *Classical Electricity and Magnetism* , Adisson-Wesley Publishing Company.

[36] Parratt, L.G., 1954. Surface studies of solids by total reflection of X-rays. *Phys. Rev.* 95:359-369.

[37] Pedersen, J.S., 1992. Model-independent determination of the surface scattering-length-density profile from specular reflectivity data. *J. Appl. Cryst.* 25:129-145.

[38] Penfold, J., and Thomas, R.K., 1990. The application of the specular reflection of neutrons to the study of surfaces and interfaces. *J. Phys. : Condens Matter.* 2:1369-

[39] Pershan, P.S., Braslau, A., Weiss, A.H., Als-Nielsen, 1987. *Phys. Rev. A* 35:4800-4813.

[40] Regan, M.J., Kawamoto, E.H., Lee, S., Pershan, P.S., Maskil, N. Deutsch, M., Magnussen, O.M., Ocko, B.M., and Berman, L.E., 1995. Surface layering in liquid Gallium: An X-ray reflectivity study. *Phys. Rev. Lett.* 75:2498-2501.

[41] Rice, S.A., Gryko, J., and Mohanty, U., 1986. In *Fluid Interfacial Phenomena*, C. A. Croxton, Edited by John Wiley & Sons Ltd, 255-342.

[42] Rodberg, L.S., and Thaler R.M., 1967. *Introduction to the Quantum Theory of Scattering*. Academic Press, New York.

[43] Russell, T.P., 1990. X-ray and neutron reflectivity for the investigation of polymers. *Mater. Sci. Rep.* 5:171-271.

[44] Sacks, P., 1993. Reconstruction of step like potentials. *Wave Motion* 18:21-30. and references therein.

[45] Sanyal, M.K., Sinha, S.K., Huang, K.G., and Ocko, B.M., 1991. X-ray scattering study of capillary-wave fluctuations at a liquid surface. *Phys. Rev. Lett.* 66:628-631.

[46] Sanyal, M.K., Sinha, S.K., Gibaud, A., Huang, K.G., Carvalho, B.L., Rafailovich, M., Sokolov, J., Zhao, X., and Zhao, W., 1992. Fourier reconstruction of the density profiles of thin films using anomalous X-ray reflectivity. *Europhys. Lett.* 21:691-695.

[47] Schiff, L.I., 1968. *Quantum Mechanics*, McGraw-Hill, New York.

[48] Schwartz, D.K., Schlossman, M.L., and Pershan, P.S., 1992. Re-entrant appearance of the phases in a relaxed Langmuir monolayer of the tetracosanoic acid as determined by X-ray scattering. *J. Chem. Phys.* 96:2356-2370.

[49] Sinha, S.K., Sirota, E.B., Garof, S. Stanely, H.B., 1988. X-ray and neutron scattering from rough surfaces. *Phys. Rev. B* 38:2297-2311.

[50] Swalen, J.D., Allra, D.L., Andrade, J.D., Chandross, E.A., Garrof, S., Israelachvilli, J., Murray, R., Pease, R.F., Wynne, K.J., and Yu, H. 1987. Molecular Monolayers and films. *Langmuir*, 3:932:950.

[51] Vaknin, D., Kjaer, K., Als-Nielsen J., and Lösche, M., 1991. A new liquid surface neutron reflectometer and its application to the study of DPPC in a monolayer at the air/water interface. *Makromol. Chem. Macromol. Symp.* 46: 383-388.

[52] Vaknin, D., Kjaer, K., Als-Nielsen, J., and Lösche, M., 1991. Structural properties of phosphotidylcholine in a monolayer at the air/water interface. Neutron reflectivity study and reexamination of X-ray reflection experiments. *Biophys. J.* 59: 1325-1332.

[53] Vaknin, D., Als-Nielsen, J., Piepenstock, M., and Lösche, M., 1991. Recognition processes at a functionalized lipid surface observed with molecular resolution. *Biophys. J.* 60: 1545-1552.

[54] Vaknin, D., Kjaer, K., Ringsdorf, H., Blankenburg, R., Piepenstock, M. Diederich, A., and Lösche, M., 1993. X-ray and neutron reflectivity studies of a protein monolayer adsorbed to a functionalized aqueous surface. *Langmuir*. 59:1171-1174.

[55] Vaknin, D., 1996. C₆₀-amine adducts at the air-water interface: A new class of Langmuir Monolayers. *Physica B*, 221:152-158.

[56] Vaknin, D., 1997. unpublished results.

[57] Vineyard, G. 1982. Grazing-incidence diffraction and the distorted-wave approximation for the study of surfaces. *Phys. Rev. B* 26:4146-4159.

[58] Wu, X.Z., Sirota, E.B., Sinha, S.K., Ocko, B.M., Deutsch, M., 1993. Surface crystalliza-

tion of liquid normal-alkanes. *Phys. Rev. Lett.* 70:958-961.

[59] Wu, X.Z., Ocko, B.M., Sirota, E.B., Sinha, S.K., Deutsch, M., Cao, B.H., and Kim, M.W., 1993. Surface tension measurements of surface freezing in liquid normal-alkanes. *Science* 261:1018-1021.

[60] Wu, X.Z., Ocko, B.M., Tang, H., Sirota, E.B., Sinha, S.K., and Deutsch, M. 1995. *Phys. Rev. Lett.* 75:1332-1335.

[61] Zhou, X.L., and Chen, S.H., 1995. Theoretical foundation of X-ray and neutron reflectometry. *Physics Reports* 257:223-348.

FIGURES

FIG. 1. The geometry of incident and scattered beam in specular reflectivity (a) and in a non-specular scattering(b) experiments.

FIG. 2. Calculated reflectivity curves for external (solid line) and internal (dashed line) scattering from an ideally flat interface versus momentum transfer given in units of the critical momentum transfer, $Q_c = 4(\pi\rho_s)^{1/2}$. The dotted line is kinematical approximation $(Q_c/2Q_z)^4$. The lower panel shows the amplitude of the wave in the medium for external (solid line) and external reflection (dashed line).

FIG. 3. Calculated reflectivities from H_2O and liquid mercury (Hg) showing the effects of absorption and surface roughness. The absorption modifies the reflectivity near the critical momentum transfer for mercury with insignificant effect on the reflectivity from H_2O . The dashed line shows the calculated reflectivity from the same interfaces with root mean square surface roughness, $\sigma = 3\text{\AA}$.

FIG. 4. An illustration of a continuous scattering length density, *sliced* into a histogram.

FIG. 5. Calculated reflectivities for two films with identical thicknesses but with two distinct normalized electron densities ρ_1 (solid line) and $1 - \rho_1$ (dashed line) and corresponding calculated reflectivities using the dynamical approach ($\sigma = 0$). The two reflectivities are almost identical except for a minute difference near the first minimum (see arrow in figure). The Born approximation (dotted line) for the two models yields identical reflectivities. The inset shows the normalized reflectivities near the first minimum. As Q_z is increased the three curves converge. This is the simplest demonstration of the phase problem, the non-uniqueness of models where two different potentials give the same reflectivities.

FIG. 6. (a) Illustration of wave paths for exterior (a) and interior(b) scatterer near a step-like interface. In both cases the scattering is enhanced by the transmission function when the angle of the incidence is varied around the critical angle. However, due to the asymmetry between external and internal reflectivity the rod scan of the final beam modulates the scattering differently as is shown on the right hand side in each case.

FIG. 7. Monochromator geometry to tilt a Bragg reflected beam from the horizon on a liquid surface. Two possible tilting configurations about the primary beam axis and about an axis along the surface of the reflecting planes are shown.

FIG. 8. Superposition of the reflected-beam (circles) below the critical angle and direct beam (triangles), demonstrating total reflectivity of X-rays from the surface of water. Severe surface roughness reduces the intensity and widens the reflected signal. A reduction from total reflectivity can also occur if the slits of the incident beam are too wide, so that the *beam-footprint* is larger than the surface sample.

FIG. 9. Experimental reflectivity from the surface of water. The dashed line is the calculated Fresnel reflectivity from an ideally flat water-interface, R_F . The Normalized reflectivity versus Q_z^2 is fitted to a the form $R/R_F = e^{-(Q_z\sigma)^2}$, demonstrating the validity of the capillary-wave model [Buff. et al., 1965].

FIG. 10. (a) Normalized X-ray reflectivity from Dihexadecyl-phosphate (DHDP) monolayer at the air-water interface with best fit electron density, N_e , shown with solid line in the inset. The calculated reflectivity from the best model is shown with a solid line. The dashed line in the inset shows the *box* model with no roughness $\sigma = 0$. (b) A diffraction from the same monolayer showing a prominent 2D Bragg reflection corresponding to the hexagonal ordering of individual hydrocarbon chains at $Q^B \perp = 1.516 \text{ \AA}^{-1}$. The inset shows a rod scan from the quasi-2D Bragg reflection at Q_\perp^B , with a calculated model for tilted chains denoted by solid line (see text for more details).

FIG. 11. Upper panel shows measured reflectivity for liquid Ga. Data marked with X were collected prior to sample cleaning whereas the other symbols correspond to clean surfaces (for details see Regan et al., 1995). Calculated Fresnel reflectivity from liquid Ga surface convoluted with a surface roughness due to capillary waves ($\sigma = 0.82 \text{ \AA}$), and the atomic form factor for Ga is denoted with a solid line. The lower panel shows the normalized reflectivity, with a solid line that was calculated with the best fit by an exponentially decaying sine model shown in the inset (Courtesy of Regan et al. 1995

TABLES

TABLE I. Electron number density, SLD, critical angles and momentum transfers, and absorption term for water and liquid mercury.

	$N_e(e/\text{\AA}^3)$	$\rho_s(\text{\AA}^{-2} \times 10^{-5})$	$Q_c(\text{\AA}^{-1})$	α_c (deg.) for $\lambda = 1.5404\text{\AA}$	$\beta(\times 10^{-8})$
H ₂ O	0.334	0.942	0.02176	0.153	1.2
Hg	3.265	9.208	0.06803	0.478	360.9

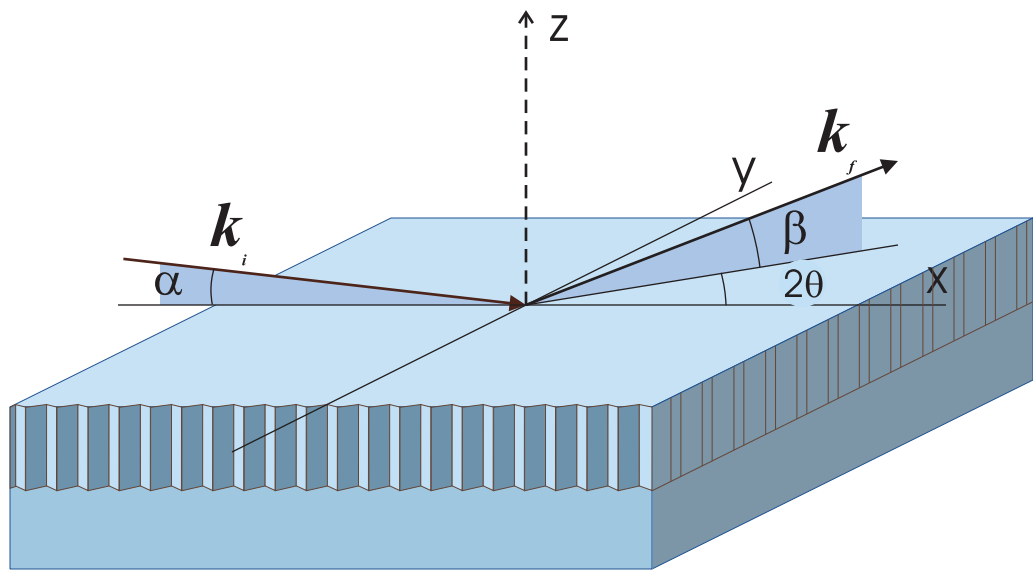
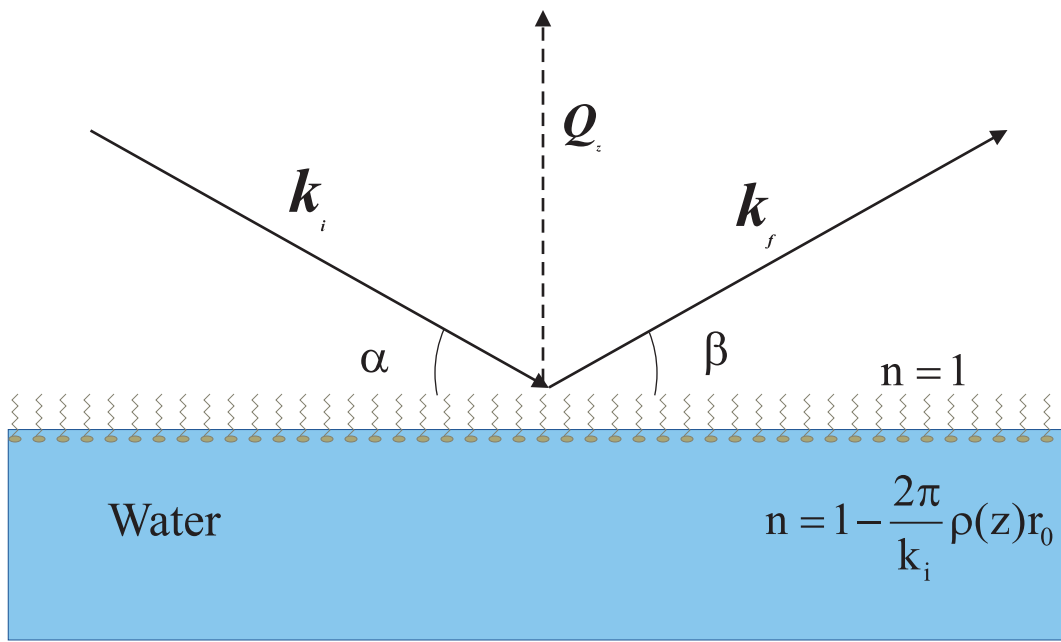


Figure 1

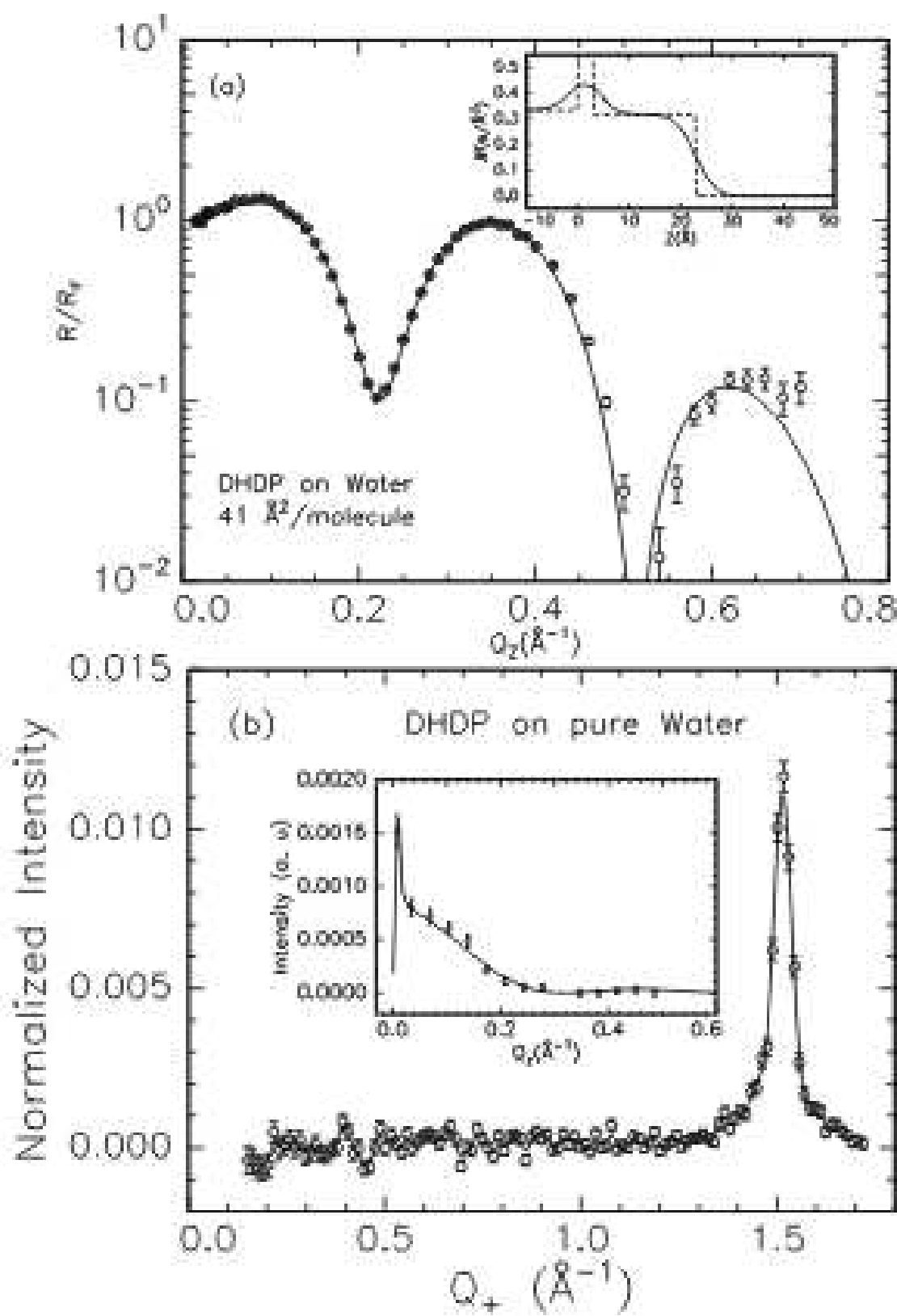
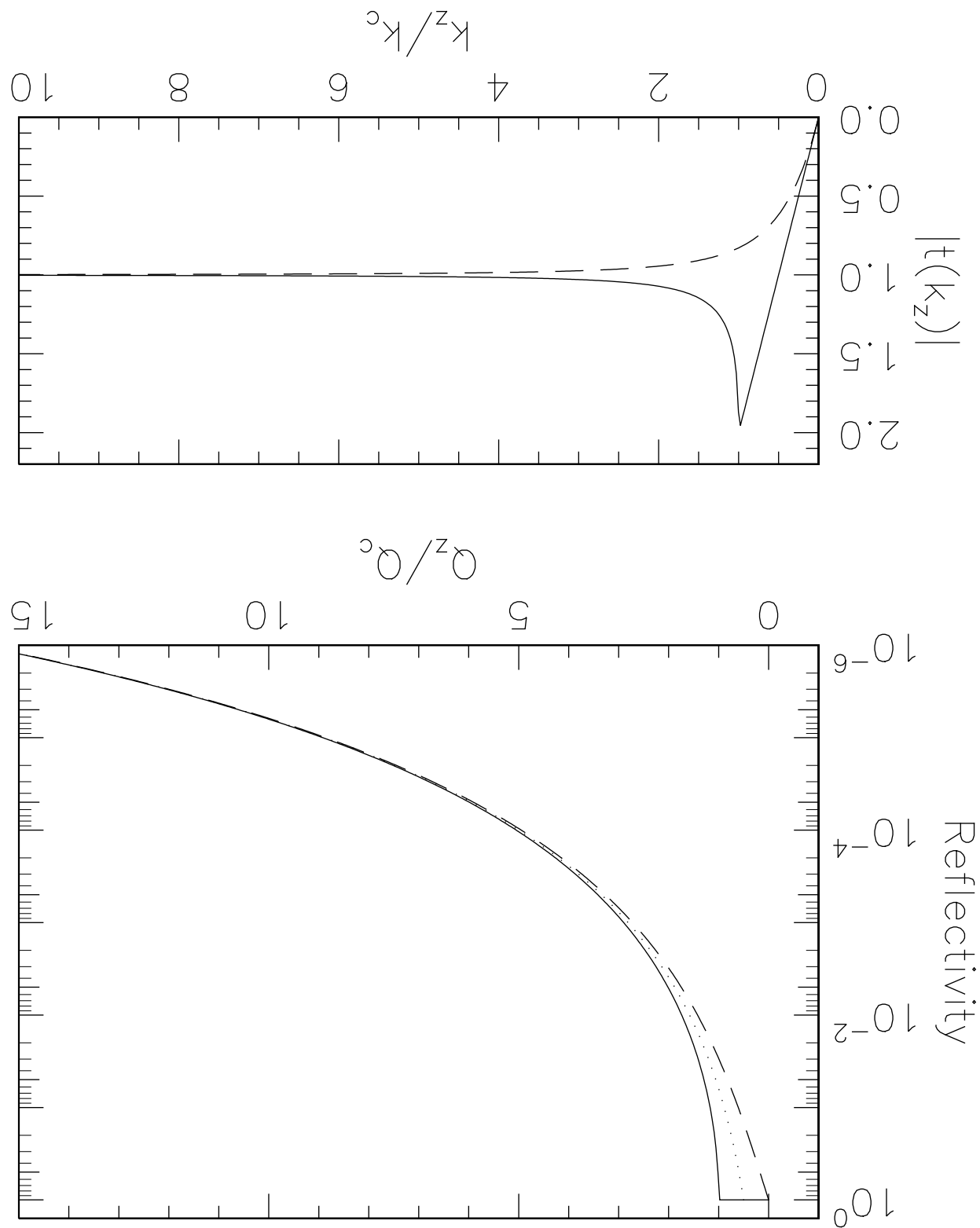


Figure 10



R

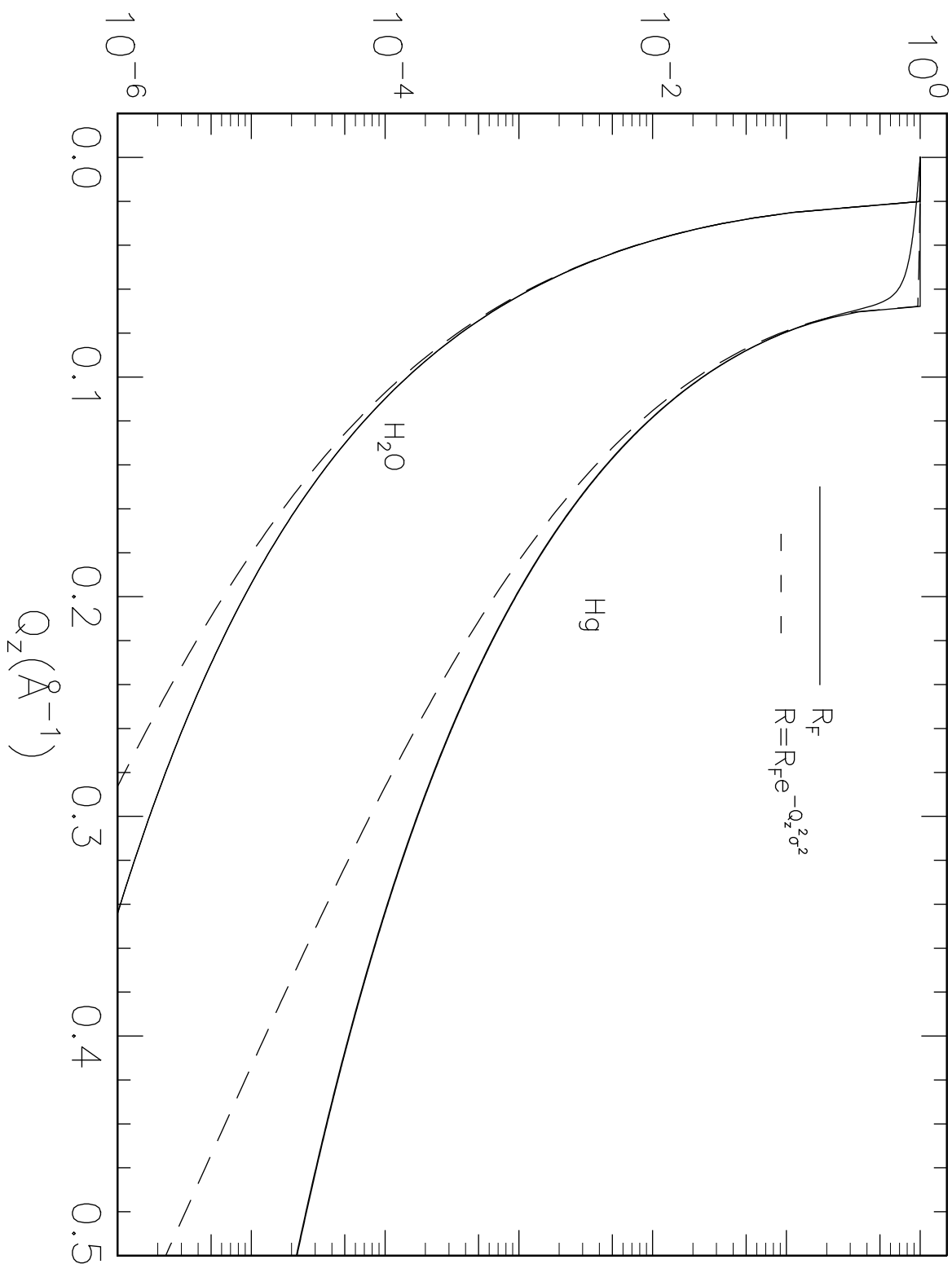


Figure 3 c:/david/reflec/figure3.ma

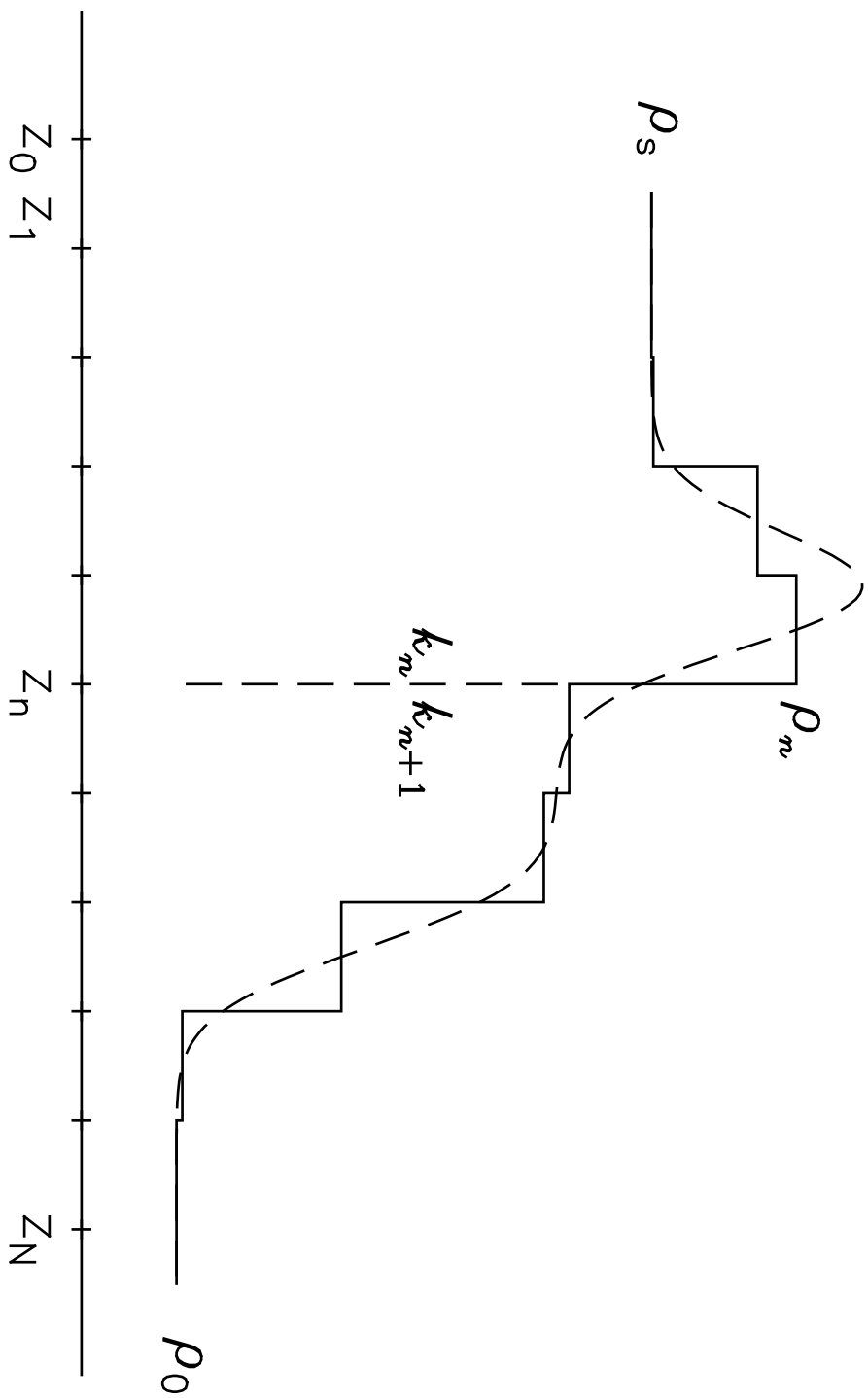
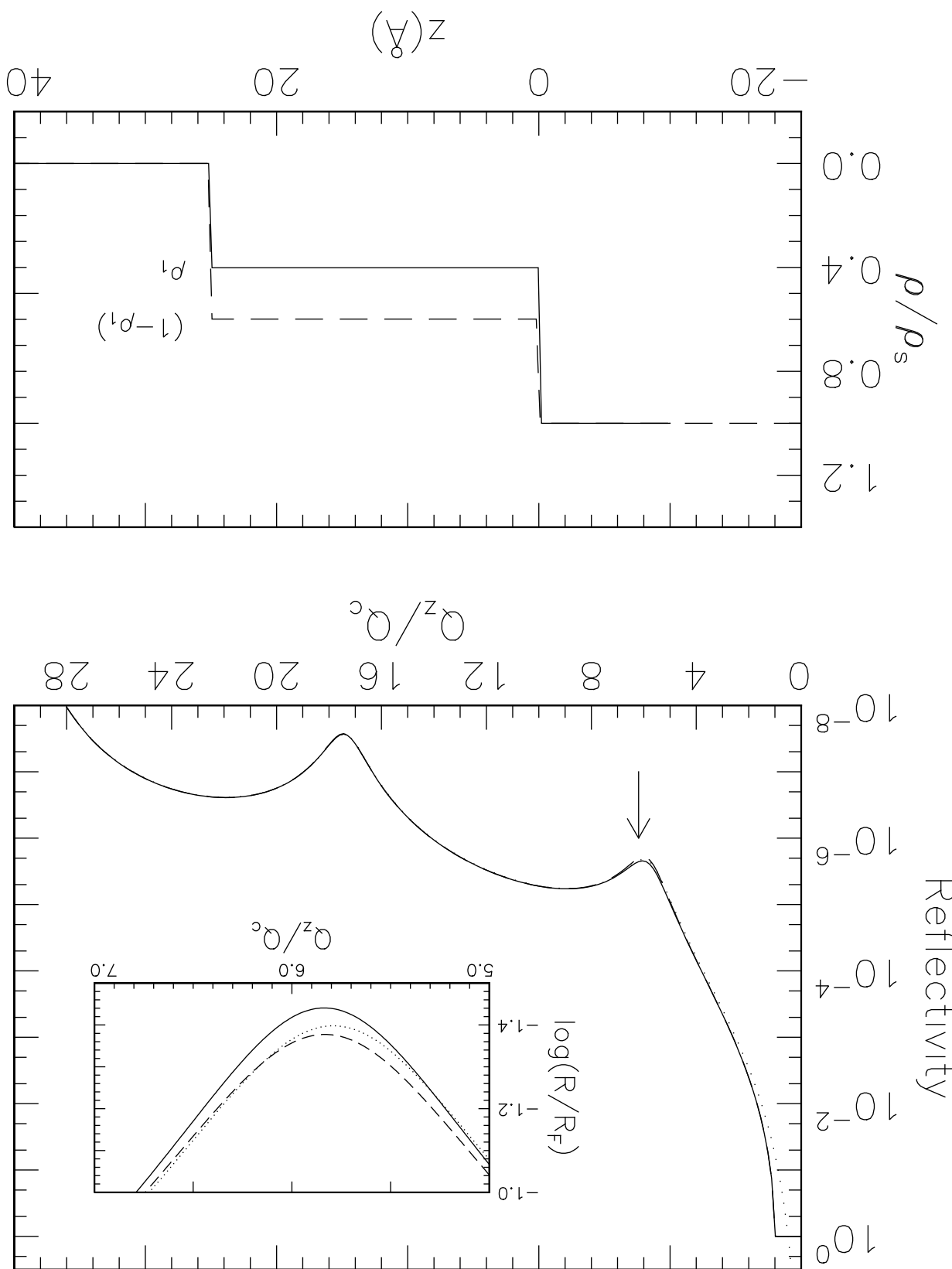
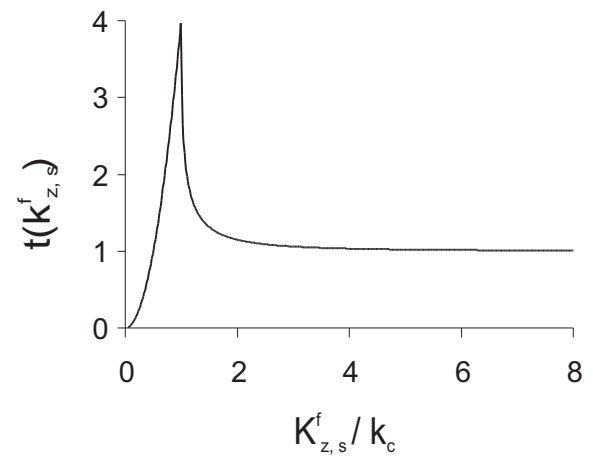
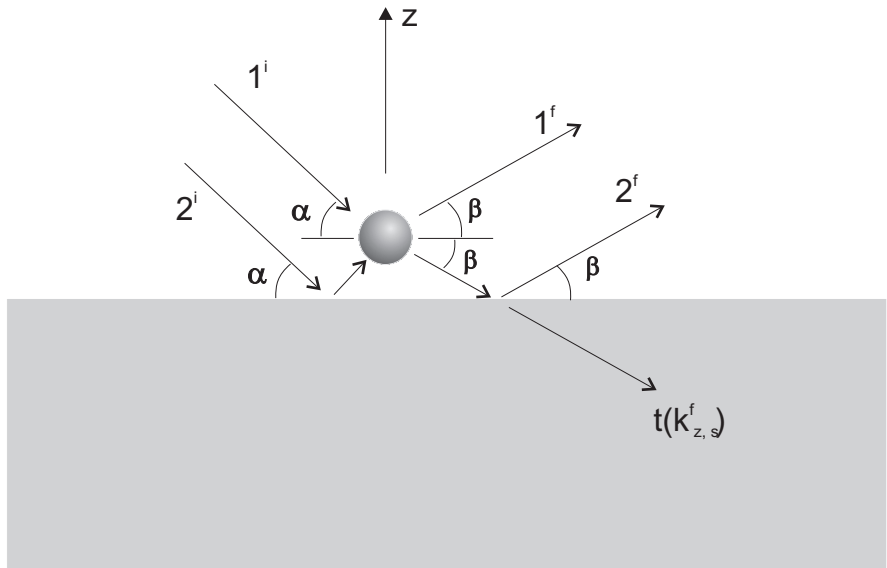


Figure 4
c:/david/reflec/figure4.ma



(a)



(b)

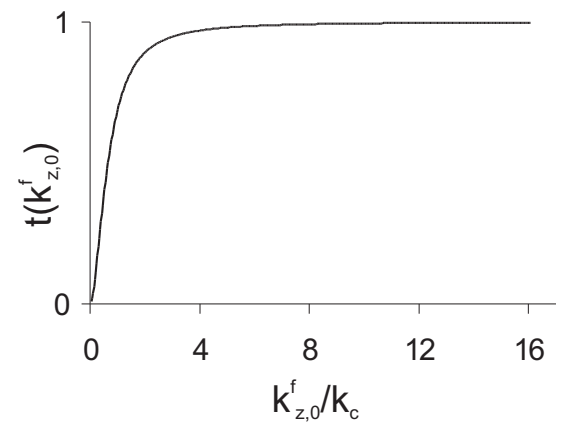
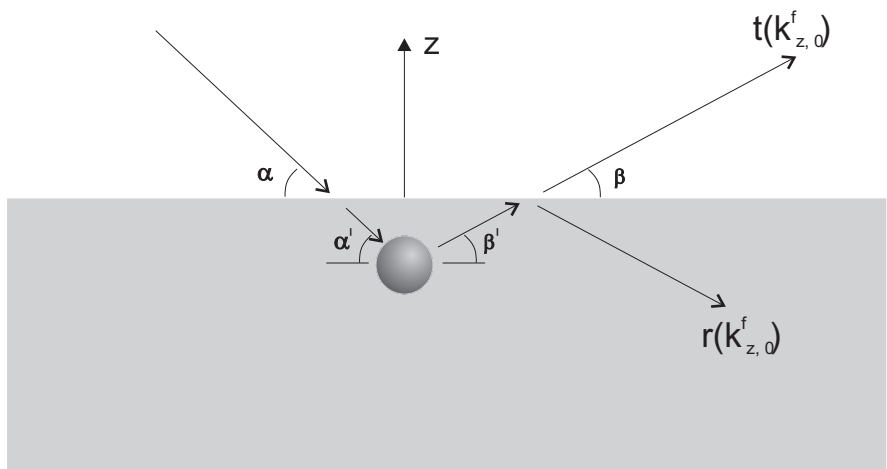
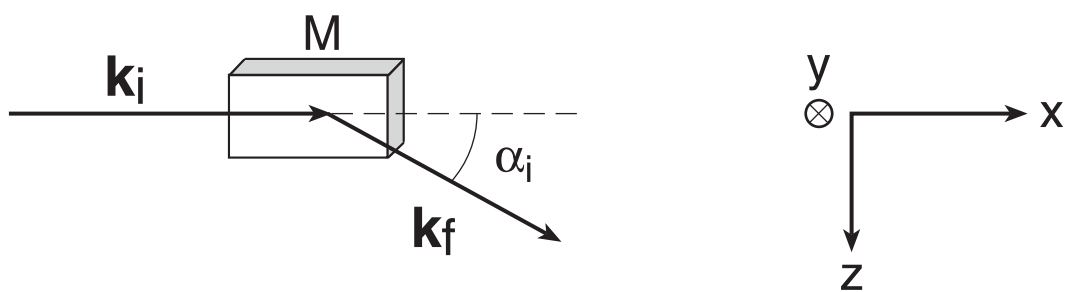


Figure 6

Side View



Top View

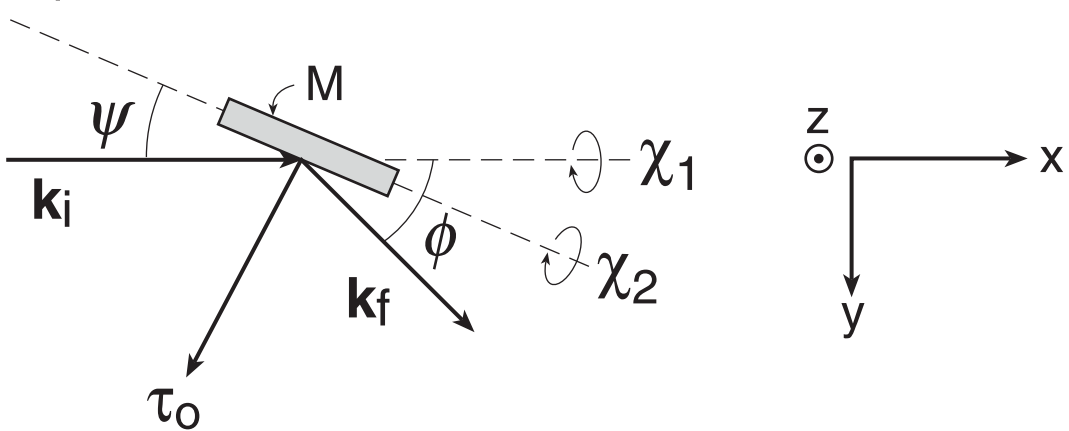


Figure 7

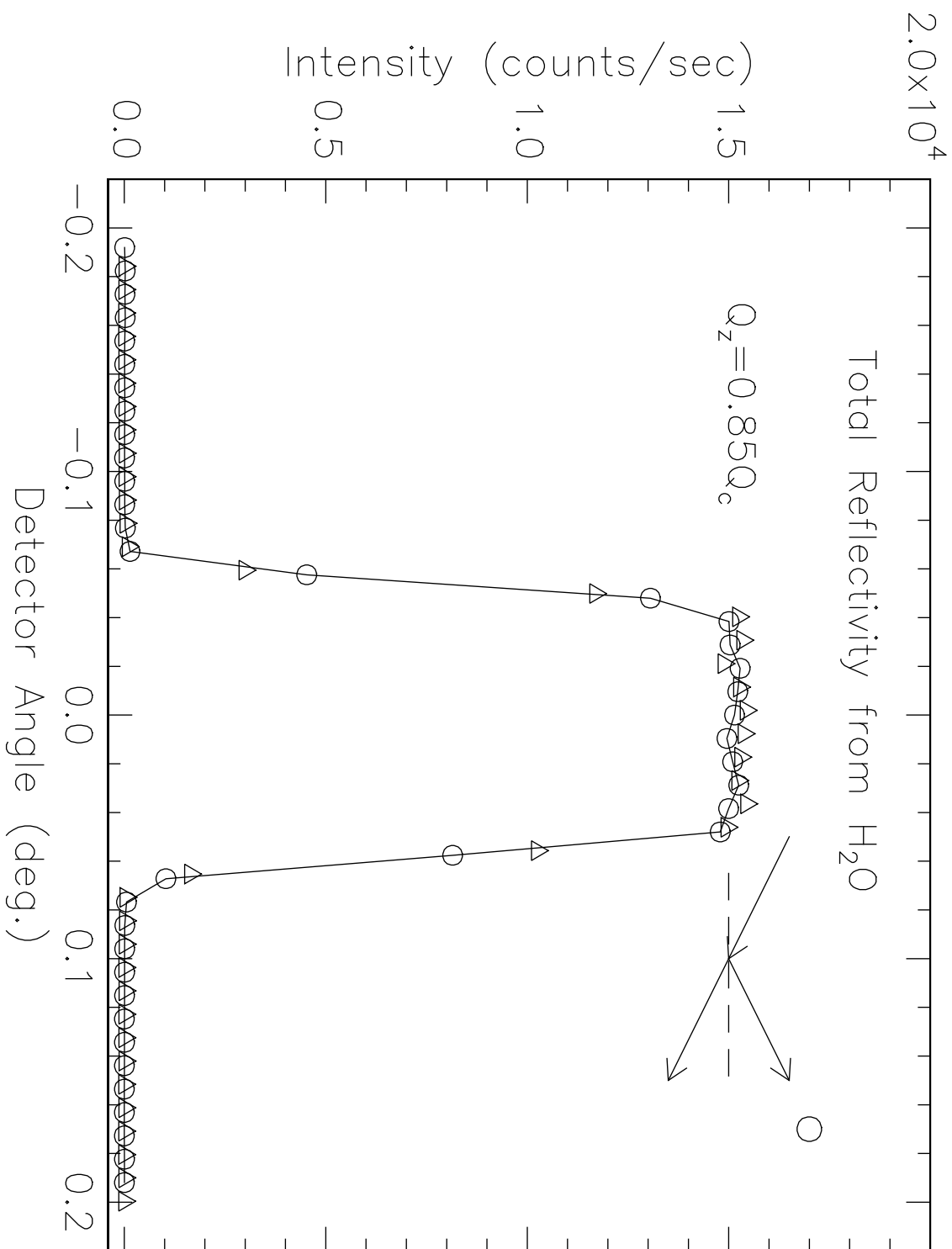
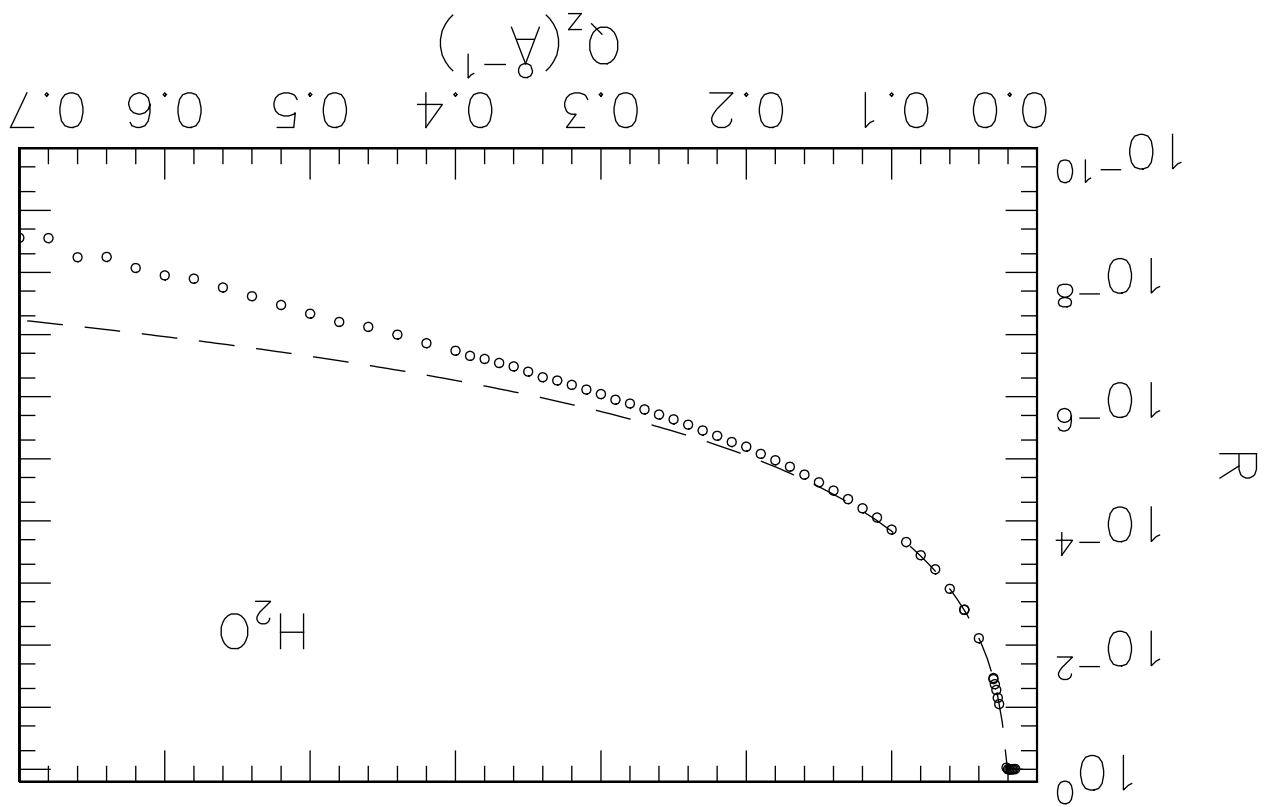
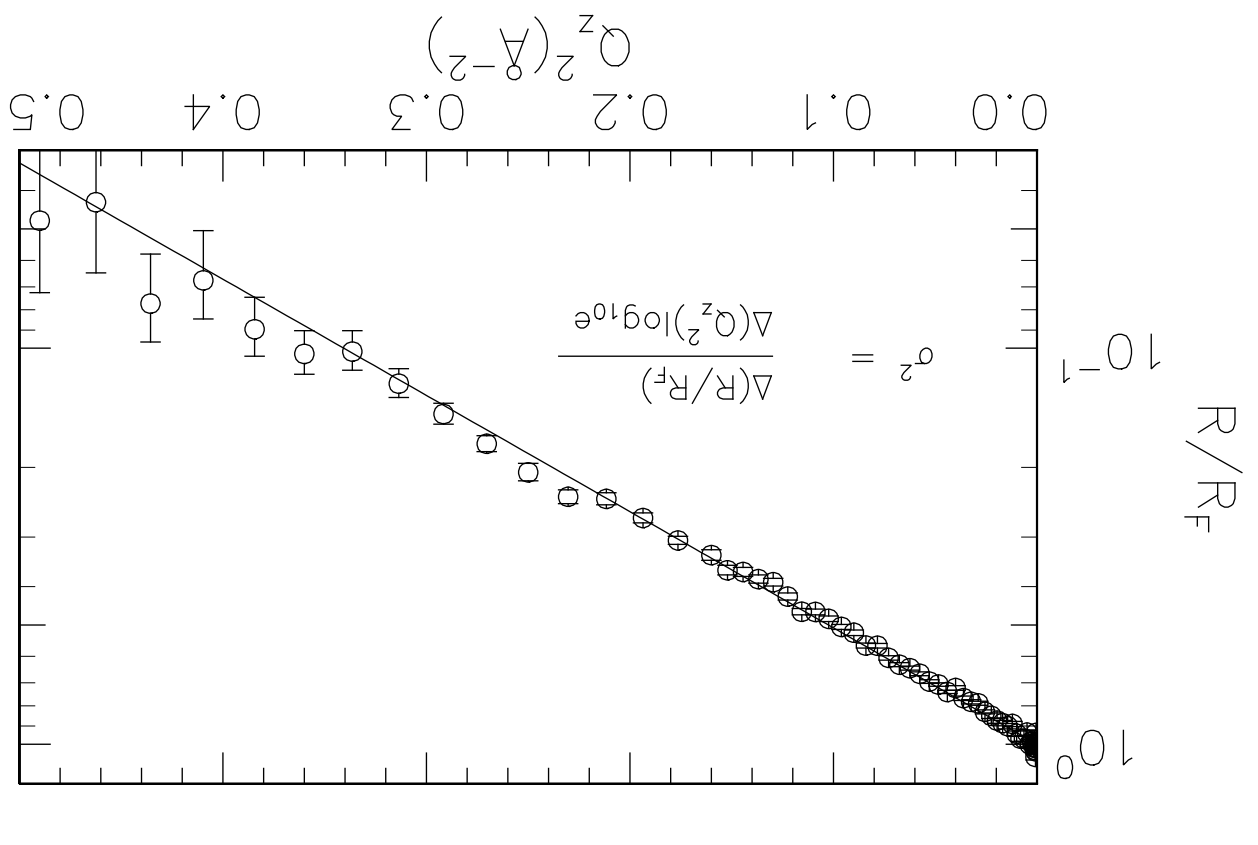


Figure 7 c:/david/reflec/figure7.mac



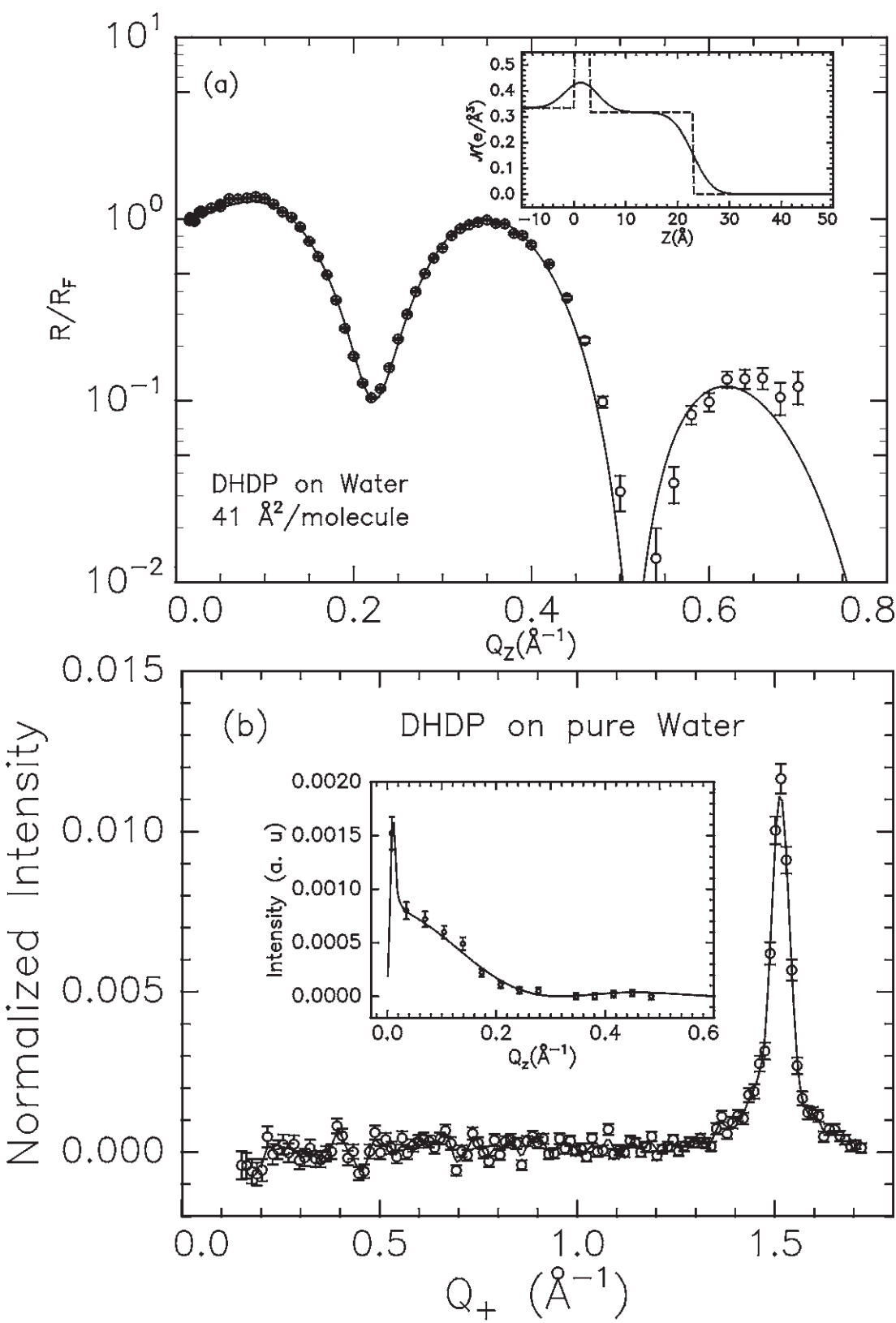


Figure 10

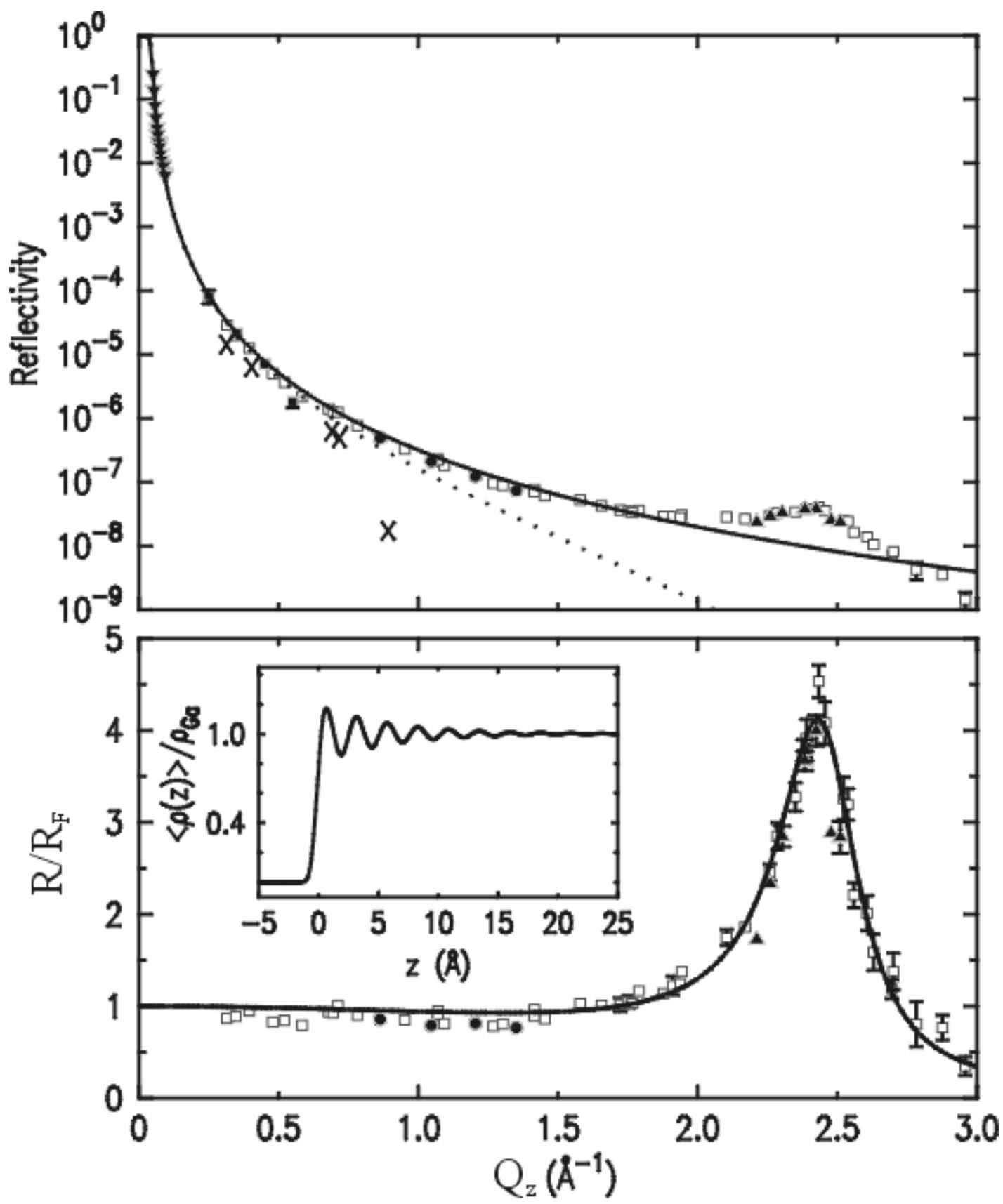


Figure 11